Check for updates

JGR Planets

RESEARCH ARTICLE
10.1029/2025JE009105

Following the HCl Cycle Over Three Martian Seasons in Mars Year 36

Sara Faggi[1,2], Shohei Aoki[3,4], Giuliano Liuzzi[5], Geronimo Villanueva[2], Hideo Sagawa[6], Michael J. Mumma[2,7], Ann Carine Vandaele[8], Frank Daerden[8], and Sébastien Viscardy[8]

[1]American University, Washington, DC, USA, [2]NASA Goddard Space Flight Center, Greenbelt, MD, USA, [3]Department of Complexity Science and Engineering, Graduate School of Frontier Sciences, The University of Tokyo, Kashiwa, Japan, [4]Department of Geophysics, Graduate School of Science, Tohoku University, Sendai, Japan, [5]Scuola di Ingegneria, Università degli Studi della Basilicata, Potenza, Italy, [6]Faculty of Science, Kyoto Sangyo University, Kyoto, Japan, [7]Department of Astronomy, University of Maryland, College Park, MD, USA, [8]Royal Belgian Institute for Space Aeronomy, Brussels, Belgium

Key Points:

- High-resolution ground-based spectroscopy was used to map Hydrogen chloride (HCl) in the Martian atmosphere over three seasons of Mars Year 36
- While water vapor is directly correlated with HCl, the role of dust appeared complex, suggesting the presence of two competing processes
- Enhancements of HCl abundances were observed around mid-equatorial latitudes during Equinoxes

Correspondence to:
S. Faggi,
sara.faggi@nasa.gov

Citation:
Faggi, S., Aoki, S., Liuzzi, G., Villanueva, G., Sagawa, H., Mumma, M. J., et al. (2025). Following the HCl cycle over three Martian seasons in Mars year 36. *Journal of Geophysical Research: Planets*, *130*, e2025JE009105. https://doi.org/10.1029/2025JE009105

Received 24 MAR 2025
Accepted 28 OCT 2025

Author Contributions:
Conceptualization: Sara Faggi, Shohei Aoki, Geronimo Villanueva
Data curation: Sara Faggi
Formal analysis: Sara Faggi
Investigation: Sara Faggi, Shohei Aoki, Giuliano Liuzzi, Geronimo Villanueva, Hideo Sagawa, Michael J. Mumma
Methodology: Sara Faggi
Resources: Geronimo Villanueva
Software: Geronimo Villanueva
Supervision: Geronimo Villanueva
Validation: Geronimo Villanueva
Writing – original draft: Sara Faggi
Writing – review & editing: Shohei Aoki, Giuliano Liuzzi, Geronimo Villanueva, Hideo Sagawa, Michael J. Mumma, Ann Carine Vandaele, Frank Daerden, Sébastien Viscardy

© 2025. American Geophysical Union. All Rights Reserved.

Abstract Hydrogen chloride (HCl) was recently discovered in the Mars atmosphere using the ESA's ExoMars Trace Gas Orbiter (TGO) onboard ESA's ExoMars mission. Its discovery is the first confirmation of an active presence of any chlorine-bearing species in the modern Mars atmosphere. TGO permitted investigations of HCl altitude profiles with high precision and showed that water vapor and ice clouds play an important role in the production and temporary loss of HCl. TGO cannot always sample the Martian atmosphere near the surface, and when those measurements are possible, they are highly affected by the increase in dust opacity, nor can TGO observe at equatorial latitudes with high cadence, due to orbital constraints, so its measurements are not suitable to obtain instantaneous global coverage. In this work, we present a methodic investigation of the Martian atmosphere, in support of the ExoMars TGO mission, targeting HCl and water using iSHELL at NASA/InfraRed Telescope Facility. Our observations mapped the Martian atmosphere, exploring three seasons in Martian Year 36. We observed the beginning of an increase in the HCl abundances around $L_S = 249°–301°$, followed by a drop in the abundances around $L_S = 319°$. We confirmed a strong correlation between the spatial distribution of water vapor and HCl—both globally and locally—suggesting that water vapor plays an important role in the production of HCl, in agreement with previous studies. Our observations also suggest the presence of two competing processes involving the dust, one supporting HCl production and another one contributing to its destruction.

Plain Language Summary Hydrogen chloride (HCl) was recently discovered in the atmosphere of Mars using the two spectrometers on board ESA's ExoMars Trace Gas Orbiter (TGO) mission. This discovery confirmed the presence of chlorine species in the modern Martian atmosphere and demonstrated the presence of an unknown active chlorine chemistry. TGO can provide highly detailed information on the vertical structure of the Martian atmosphere by studying the interplay of the gaseous species across the atmosphere structure, but it cannot provide instantaneous complete hemispheric coverage. To study the spatial distribution of the possible sources and sinks of HCl, and to support the ExoMars TGO mission, we therefore performed methodic ground-based observations, mapping the Martian atmosphere and systematically exploring three Martian seasons in Martian Year 36.

1. Introduction

Decades of space exploration, both orbital and in situ have provided extensive knowledge of the surface and atmosphere of Mars (Montmessin et al., 2024; M. D. Smith, 2008). Data acquired over time by dedicated missions (e.g., NASA/Mars Atmosphere and Volatile EvolutioN, ESA/Mars Express, ESA/ExoMars) along with Earth-based observing campaigns (e.g., ESO/Very Large Telescope (VLT), W. M. Keck Observatory, NASA/InfraRed Telescope Facility (IRTF)) have significantly improved our understanding of the present and past atmosphere of Mars (Encrenaz et al., 2004, 2019; A. Fedorova et al., 2023; A. A. Fedorova et al., 2020; O. Korablev et al., 2019; O. I. Korablev et al., 2001; Montmessin et al., 2004, 2022; M. D. Smith, 2002; M. D. Smith et al., 2006, 2018, 2022; Trokhimovskiy et al., 2015; Vandaele et al., 2024), its volatile loss (Villanueva et al., 2015), and its seasonal atmospheric cycle (Aoki et al., 2022; Crismani et al., 2021; Daerden et al., 2022; Liuzzi et al., 2020; Villanueva, Liuzzi, Aoki, et al., 2022). However, our understanding of the evolution of trace gases over time, and the relation between surface and atmospheric chemistry, remains limited.

21699100, 2025, 11, Downloaded from https://agupubs.onlinelibrary.wiley.com/doi/10.1029/2025JE009105 by Sara Faggi - Nasa Goddard , Wiley Online Library on [14/11/2025]. See the Terms and Conditions (https://onlinelibrary.wiley.com/terms-and-conditions) on Wiley Online Library for rules of use; OA articles are governed by the applicable Creative Commons License

Mars has a complex and diverse chemical history. Understanding its evolution and potential habitability requires examining its chemical inventory, including trace species like hydrogen chloride (HCl). These compounds might be related to past atmospheric processes and could provide hints on atmospheric evolution. While the modern Martian atmosphere is in an oxidizing state and its photochemistry is dominated by CO_2, H_2O, and their photochemical products (V. Krasnopolsky & Lefèvre, 2013), this has not always been the case in the past. In its early history, Mars likely went through a significantly different atmospheric chemistry with a reducing atmosphere characterized by the presence of volcanic activity and related product species (Catling & Moore, 2003; Sholes et al., 2017; S. C. Solomon et al., 2005; Zahnle et al., 2008).

On Earth, volcanism emits mostly oxidized volatiles (CO_2, CO, H_2O, and SO_2), smaller amounts of reduced gases (H_2 and H_2S), and trace amounts of other species (S_2, HCl, HF, OCS, and SO) (S. Solomon, 1999). Despite the unknown oxidation state of the ancient Martian atmosphere, it is widely believed that volcanic outgassing was likely rich in sulfur-bearing species, with their abundances depending on the chemical state of Martian magmas—specifically their redox conditions, water content, and the abundances of sulfur and carbon (Gaillard & Scaillet, 2009; Sholes et al., 2017). This is supported by the widespread presence of sulfate deposits in both soils and rocks, as detected by in situ rover investigations: by the Viking lander (Toulmin et al., 1977), by the Mars Exploration Rovers (Squyres et al., 2006), by Phoenix (Kounaves et al., 2010), Mars Science Laboratory (Mahaffy et al., 2013), and by recent searches from ExoMars Trace Gas Orbiter (TGO) (Braude et al., 2022). Further evidence came from the detection of S-bearing volatiles (SO_2, H_2S, OCS, and CS_2) through in situ evolved gas analysis performed by the Sample Analysis at Mars (McAdam et al., 2014).

While chlorine-bearing species such as HCl are minor volcanic byproducts on Earth, they play a crucial role in terrestrial stratospheric ozone depletion (S. Solomon, 1999). On Mars, perchlorate salts (ClO_4^-) and chloride-bearing minerals Cl^- are known to be widely present on the surface (Catling et al., 2010; Glavin et al., 2013; Hecht et al., 2009; Osterloo et al., 2008; M. L. Smith et al., 2014). However, chlorine chemistry—and its overall role in the atmospheric cycle on both modern and ancient Mars—was previously thought to play a minor role due to the lack of HCl detections in the atmosphere (Hartogh et al., 2010; V. A. Krasnopolsky et al., 1997; Villanueva et al., 2013).

This view has recently changed. HCl, the main reservoir of atmospheric chlorine, was discovered at levels of ∼4 parts per billion by volume (ppbv) in the Martian atmosphere by the Atmospheric Chemistry Suite (ACS) and the Nadir and Occultation for Mars Discovery (NOMAD) spectrometers onboard ESA's ExoMars TGO mission (Aoki et al., 2021; O. Korablev et al., 2021; Liuzzi et al., 2021; Olsen et al., 2021, 2024a, 2024b; Trokhimovskiy et al., 2021). This discovery provided the first direct evidence of chlorine-bearing species in the modern Martian atmosphere. Importantly, the detection of HCl does not imply ongoing volcanic activity on Mars. HCl has been detected simultaneously at widely separated locations, and no correlated outgassing of sulfur-bearing species has been observed (Braude et al., 2022; Khayat et al., 2015). This finding demonstrated the presence of active—but still poorly understood—chlorine chemistry in the modern atmosphere, and triggered a revision of photochemical and climatological modeling of chlorine-bearing species in the Martian atmosphere (V. A. Krasnopolsky, 2022; Rajendran et al., 2025; Streeter et al., 2025; Taysum et al., 2024a).

ExoMars/TGO observations also revealed the seasonality of HCl release in the Martian atmosphere, showing a strong correlation with the water cycle (Aoki et al., 2021, 2024; Olsen et al., 2021, 2024a, 2024b) and, at times (though not always) with the presence of dust. HCl abundances appear to increase at the beginning of the southern summer ($L_S \sim 240°$), when large amounts of dust are also lifted into the atmosphere. It subsequently decreased rapidly at the end of this season and at the end of the dusty period ($L_S \sim 320°$). This behavior was first observed in Martian Year (MY) 34, which was characterized by a Global Dust Storm, initially suggesting a correlation between HCl release and such a planet-wide storm. However, the same seasonal pattern was observed again in MY 35, which did not experience a global dust storm but still exhibited the usual seasonal increase in dust abundance in the atmosphere across the southern summer period. That pointed to the fact that the HCl cycle is more closely connected with the seasonal release of water vapor from the southern polar cap, rather than being driven solely by dust activity (Aoki et al., 2021; Olsen et al., 2021, 2024a, 2024b). HCl signatures were recovered at $L_S \sim 90°$–110° at a level of about ∼2 ppb. These were obtained from a re-analysis of the ACS data set after improving their data reduction, suggesting a possible release of HCl in the northern summer season but at a lower abundance rate relative to the southern summer season. The asymmetric behavior between the northern and southern summers still remains unclear (Olsen et al., 2024a, 2024b).

21699100, 2025, 11, Downloaded from https://agupubs.onlinelibrary.wiley.com/doi/10.1029/2025JE009105 by Sara Faggi - Nasa Goddard , Wiley Online Library on [14/11/2025]. See the Terms and Conditions (https://onlinelibrary.wiley.com/terms-and-conditions) on Wiley Online Library for rules of use; OA articles are governed by the applicable Creative Commons License

Table 1
Previous Mars Observations Targeting HCl and Their Observing Requirements

Previous observations	Mars year and season [°]	Spectral resolution	Spatial resolution
FTS/Kitt Peak[a]	MY 18, $L_S = 223$	$R \sim 27{,}000$	6.5″ (Mars diameter 13″)
HIFI/Herschel[b]	MY 30, $L_S = 76$–78	$R \sim 1{,}000{,}000$	11″ (Mars diameter 8″)
CSHELL/IRTF[c]	MY 27, $L_S = 352$	$R \sim 50{,}000$	0.5″ × 30″[d]
CRIRES/VLT[c]	MY 29, $L_S = 324$	$R \sim 90{,}000$	0.2″ × 40″[d]
	MY 30, $L_S = 12$	$R \sim 90{,}000$	

[a]Krasnopolsky et al., 1997. [b]Hartogh et al., 2010. [c]Villanueva et al., 2013. [d]Spatial resolution for these observations is not defined by the diffraction limit, but it is seeing limited.

Before its discovery by TGO, HCl had been extensively searched in the Martian atmosphere (as summarized in Table 1). The first observation, performed in 1997 targeted a possible premature period for the release of HCl (V. A. Krasnopolsky et al., 1997). Moreover, even though the instrument had enough spectral resolution to distinguish the Mars HCl lines relative to the telluric absorptions, it lacked spatial resolution, as it was only capable of taking mean hemispheric spectra. The second attempt was again primarily focused outside the HCl season—as now identified by TGO observations. Additionally, the instrument employed only provided disk-average data, strongly diluting any possible present spectral feature (Hartogh et al., 2010). Lastly, observations using CRIRES/VLT and CSHELL/IRTF—despite the excellent capabilities of the two spectrometers both in spatial and spectral resolution—failed to detect HCl. These observations were conducted across three distinct solar longitudes, $L_S = 324°$, 352°, 12°, revealing upper limits of HCl abundances <1.5, 2.1, and 0.6 ppb, respectively (Villanueva et al., 2013). Two of these observations ($L_S = 352°$ and 12°) fell outside the period of significant HCl abundances. Finally, in the case of the observations at $L_S = 324°$, the HCl line (~2,981 cm^{-1}) within the spectral region sampled by CRIRES was blended with CO_2 absorption and a solar feature.

ExoMars/TGO has enabled the investigation of vertical profiles of HCl and water vapor with high precision, allowing studies of HCl's interplay with water vapor and with the formation of water ice clouds. However, it cannot always accurately sample the Martian atmosphere near the surface due to the increase in dust opacity, nor it can observe at equatorial latitudes with high cadence due to orbital constraints. Thus, the ACS and NOMAD solar occultation measurements are not suited to providing temporally regular global coverage.

In this work, we present a methodic investigation of the Martian atmosphere, targeting HCl, water and trace gases using a high-resolution near infrared echelle spectrometer (iSHELL) installed at the NASA IRTF. Our study systematically explored the solar longitudes available from the ground in MY36, enabling us to investigate the HCl cycle across three Martian seasons. One of the advantages of using ground-based telescopes is their ability to capture a snapshot of the planet, allowing to explore all latitudes. Therefore, by obtaining temporally global hemispheric maps of the Martian atmosphere, we could spatially identify the beginning and the end of the HCl cycle, investigate its temporal variability, and compare its spatial distribution with that of water and dust.

2. Observations and Data Analysis

The Mars observing campaign took place over two years, in 2021 and 2022, and immediately following the first two operations conducted as part of Director Discretionary Time (DDT) in September and November of 2020. These first two DDT operations targeted the Martian southern summer season in MY35, during which we tested the feasibility of the measurements, recovered the HCl signature, and confirmed the TGO discovery (Aoki et al., 2024). The subsequent two years of observations spanned three Mars seasons across MY36, aiming to study how water releases influence HCl production and to investigate the chlorine cycle. Details of these observations are reported in Table 2, with a graphic summary shown in Figure 1.

In the first semester of 2021, the Martian seasons ranged from $L_S \sim 0°$ (Spring Equinox in the North Hemisphere) in early February to $L_S \sim 79°$ at the end of July. We therefore planned for eight observing runs sampling different Solar Longitudes: $L_S = 0°$, 25°, 50°, and 75° (see Table 2, and Figure 1). This strategic seasonal sampling was primary designed to target HCl during the pre-northern summer period and investigate its connection with the Martian atmospheric water cycle, since the Northern Polar Cap starts sublimating around $L_S \sim 70°$. This would

21699100, 2025, 11, Downloaded from https://agupubs.onlinelibrary.wiley.com/doi/10.1029/2025JE009105 by Sara Faggi - Nasa Goddard , Wiley Online Library on [14/11/2025]. See the Terms and Conditions (https://onlinelibrary.wiley.com/terms-and-conditions) on Wiley Online Library for rules of use; OA articles are governed by the applicable Creative Commons License

Table 2
Observing Summary

Date	Mars diameter [″]	Seeing [″]	Number of slit positions	Sampled area[a] [km^2]	CML [°]	L_S [°]	Comments
Martian Year 35 Southern Summer							
7 September[b] 20	19	0.8	10 North and10 South	129 × 170	35.9	273	HCl season
1 November[b] 20	20	0.8	10 North and10 South	127 × 168	236.4	306	″
2 February 21	---------- no data, bad weather ----------						
21 February 21	6.6	0.6	5	378 × 499	296.2	7.7	Northern spring ($Ls = 0$)
22 March 21	5.6	0.7	5	454 × 599	198.2	20	HCl presence
10 April 21	5.1	0.7	5	501 × 662	23.5	29	″
18 May 21	---------- seeing 2.5–3″, no map available ----------						
6 June 21	4.1	1.5	3	622 × 821	272.9	55	North polar cap starts sublimating
24 June 21	---------- seeing 2.5–3″, no map available ----------						
14 July 21	3.7	1.0	3	678 × 894	293.9	75	Reappearance of HCl?
Martian Year 36 Northern Summer							
Mars was not observable							
Martian Year 36 Pre–Southern Summer							
31 March 22	5.2	0.8	5	493 × 651	39.7	200	Southern spring ($L_s = 180°$)
21 April 22	5.6	0.6	7	459 × 606	226.3	213	
29 May 22	6.4	0.8	7	401 × 529	247.0	236	South polar cap starts sublimating
18 June 22	6.9	0.8	7	372 × 491	76.9	249	Beginning of peak HCl activity
7 July 22	7.4	0.8	7	344 × 455	285.2	260	″
Martian Year 36 Southern Summer							
27 July 22	7.9	0.8	7	315 × 416	113.1	274	Southern summer ($L_s = 270°$)
10 August 22	8.7	0.7	9	295 × 389	292.8	282	HCl season
30 August 22	---------- no data, technical issues ----------						
5 September 22	10	0.8	9	254 × 336	182.4	301	″
25 September 22	12	0.8	10	223 × 294	23.9	313	Ending HCl season?
11 October 22	13	0.8	10	198 × 261	196.8	319	″
30 October 22	---------- no data, technical issues ----------						

Note. Columns report: UT dates of our observations, Mars angular diameter [″], atmospheric seeing measured for that night [″], numbers of mapping steps adopted across the disk, Central Meridional Longitude (CML in °) and the Mars Solar Longitude (L_S in °). [a]Spatial resolution in km for each spectrum extracted along the slit over a 3 × 3 pixel box, corresponding to 0.375″ × 0.495″ are reported. We adopted an iSHELL plate scale of 0.125 ″/pix in the dispersion direction and of 0.165 ″/pix in the cross-dispersion direction. [b]Director Discretionary Time (DDT) operations. Results and analysis are presented in Aoki et al., 2024. We report these operations only to compare southern Summer in MY35 with MY36 to confirm the HCl reappearance and investigate the beginning of the HCl season.

test the suggested correlation between the water and HCl release during a season that had been less explored. In the second semester of 2021, Mars was not visible for ground-based observations as its solar phase angle <20°.

In 2022, Mars was observable throughout the year. The IRTF observing schedule is divided in two semesters. During the first semester (2022A), observations targeted the Martian pre-southern summer period from $L_S \sim 180°$ (Spring in the southern hemisphere) in early February to $L_S \sim 270°$ at the end of July (summer in the southern hemisphere). We therefore planned six observations sampling different Solar Longitudes: $L_S = 200°$, 240° and 270°. This time, our primary objective was to characterize the beginning of the HCl seasonal cycle, expected to start around $L_S \sim 250°$, and gain insights into its chemistry and spatial distribution across the planet. Our secondary objective was to estimate the water release, since the southern Polar Cap starts vapourizing around

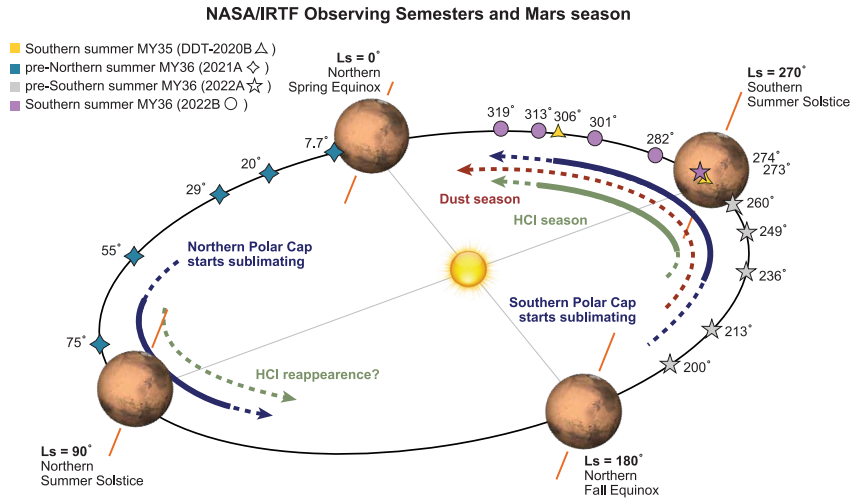

Figure 1. Observational operations with the NASA InfraRed Telescope Facility facility across the Martian Year (MY) MY 36 (from February 2021 to October 2022), covering three Martian seasons to investigate the Hydrogen chloride (HCl) appearance and disappearance. Mars was not observable between the northern summer ($L_S = 90°$) to the Northern Fall Equinox ($L_S = 180°$), corresponding to the second half of 2021. For comparison, two additional operations performed as part of Director Discretionary time during the MY35 (in 2020) are also shown, as part of our initial work in recovering the HCl signature following its first detection by Trace Gas Orbiter (Aoki et al., 2024).

$L_S \sim 230°$ and therefore confirm the suggested correlation with the beginning of the HCl season in the southern summer.

The second semester (2022B) sampled the Martian southern summer season, from $L_S \sim 277°$ in early August to $L_S \sim 0°$ in January 2023. During this period, we conducted six observing runs, focusing on the Solar Longitude intervals in which HCl is expected to reach its peak $L_S \sim 275°$ and subsequently disappear around $L_S \sim 330°$. These observations allowed to properly characterize the HCl temporal cycle and to investigate the end of the HCl season and gather information about possible sink processes and their spatial distribution. As reported in Table 2, to map both Martian hemispheres, we observed at about ∼19.3 days separation at each L_S interval. As reported in the table, only a very limited number of nights were lost due to weather, poor atmospheric conditions, or technical problems, resulting in a successful methodic investigation.

For this investigation, we used the NASA IRTF facility, which offers unique advantages for studying Mars, among other ground-based and spaceborne observatories, due to its superior daytime observing capabilities. This is made possible by the excellent performance of the guider camera, which allows accurate pointing and stable tracking—essential for mapping globally the planet. The IRTF facility hosts the long-slit near-infrared high-resolution immersion echelle spectrometer, iSHELL. Compared to previous instruments, iSHELL has broader spectral coverage and improved sensitivity, allowing to simultaneously target multiple atmospheric trace gases by using a single spectral setting. The spectrometer has a resolving power of about $\lambda/\delta\lambda = 70{,}000$ associated with the 0.375″ slit and offers selection of multiple slit widths. The six cross-dispersing gratings are mounted on a tiltable mechanism that permits selection of wavelength ranges over 15 distinct spectral settings (Rayner et al., 2012, 2022).

For our investigations, we selected the spectral setting Lp1 (∼3.2–3.6 μm), customizing the upper wavelength to 3.71 μm. This setting (which here after we will refer to as: Lp1-c) covers from 3.71 to 3.32 μm (2695.4–3,024 cm^{-1}, order 141 to 156), providing simultaneous measurements of H_2O ($2\nu_2$ band), HDO (ν_1 band), CH_4 (ν_3 band), C_2H_6 (ν_7 band), and $^{16}O^{12}C^{18}O$ ($\nu_2 + \nu_3$ band), and several other isotopic bands of CO_2. Moreover, strong lines of HCl at 2821.568, 2843.624, 2865.098, 2906.246, 2925.896, 2944.913, 2963.285, 2981.000, and 2998.046 cm^{-1} fall within multiple Lp-1c spectra orders. The Lp1-c setting allowed us to study the interconnection of HCl and water, and at the same time to probe cloud/dust scattering by measuring the CO_2 columns sampled via the CO_2 bands. For the Martian observations, we selected the narrowest slit of 0.375″ to sufficiently resolve the individual absorption lines, and for each observing run, we oriented the slit along the planet North-South direction, and we then scanned the planet across the East-West direction at steps of ∼1″. Depending on

21699100, 2025, 11, Downloaded from https://agupubs.onlinelibrary.wiley.com/doi/10.1029/2025JE009105 by Sara Faggi - Nasa Goddard , Wiley Online Library on [14/11/2025]. See the Terms and Conditions (https://onlinelibrary.wiley.com/terms-and-conditions) on Wiley Online Library for rules of use; OA articles are governed by the applicable Creative Commons License

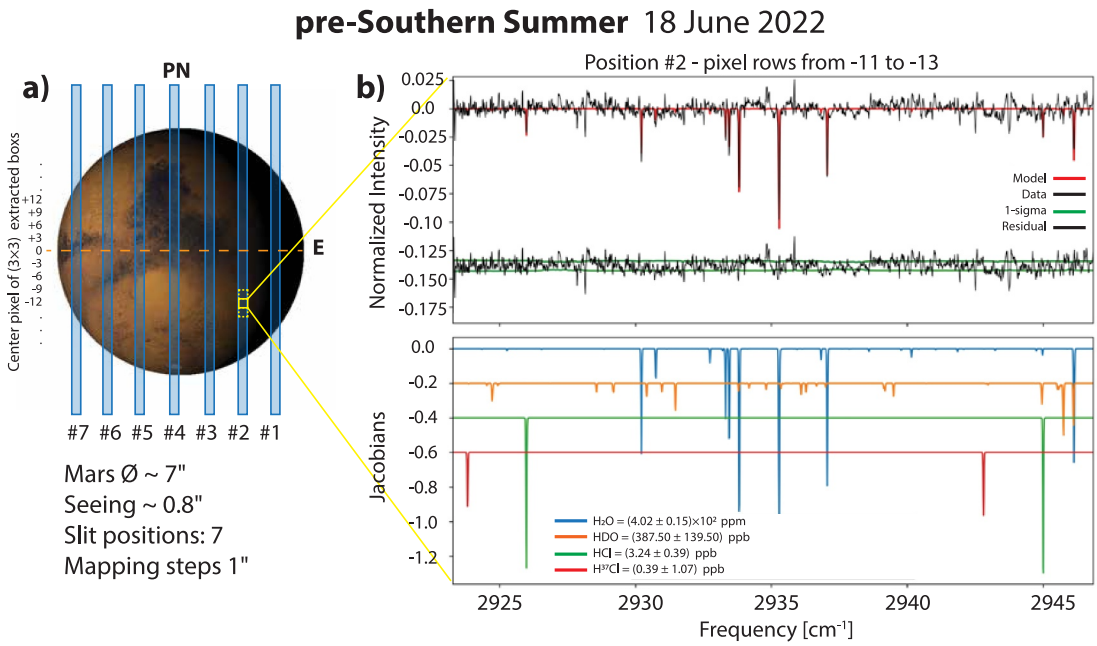

Figure 2. Panel (a) Example of mapping technique adopted on 18 June 2022. PN identifies the North Pole. Maps of the Martian disk were obtained by orienting the slit in the North-South direction and by stepping the slit across the planet at ∼1″ step, from East to West. This sequence takes about two hours when Mars is ∼10″, allowing practically almost instantaneous hemispheric mapping. Panel (b) Example of extracted spectra along the slit from a box centered on pixel −12 (yellow), so from pixel −11 to pixel −13 (dashed yellow). The upper plot shows the Mars residual spectrum (black), after telluric subtraction and solar line removal, the model of the water and Hydrogen chloride (HCl) computed with PSG is shown superimposed (red), and below the final residual. The panel below shows in multiple colors the Jacobians of the PSG OE retrieval. Two strong HCl lines are detected together with water.

the Mars angular diameter at the time of the observations, we were then able to map the planet disk with a different number of slit positions. In Figure 2a, we show an example of mapping technique.

Data presented here were processed using astroPSG.py (Villanueva et al., 2023), an advanced python-based data reduction package to process and analyze spectroscopic data. The package is built on previous highly validated IDL-based methods (DiSanti et al., 2006; Villanueva, DiSanti et al., 2012; Villanueva et al., 2011, 2013; Villanueva, Mumma, et al., 2012), and it takes advantage of new tools and analysis techniques. astroPSG allows the processing of a broad range of astronomical data, including observations of stars, planets, and small bodies. It permits spatial studies and can handle mapping schemes as needed in the case of our Mars investigations. The code has been developed employing the latest numerical and algorithmic methods to crop and extract the spectral orders, especially for high-resolution echelle data format. It performs bad-pixel correction, and spatial straightening with milli-pixel precision as well as accurate spectral calibration. astroPSG is also fully integrated with the Planetary Spectrum Generator (Villanueva et al., 2018; Villanueva, Liuzzi, Faggi, et al., 2022) and employs the PSG radiative transfer (RT) suite and models. The Python code has access to multiple climatological databases (e.g., NASA/MERRA2, Mars GCMs) and integrates the PSG retrieval package based on the Optimal Estimation method. After processing the raw echelle data and extracting the spectra across multiple iSHELL spectral orders, the main components of our data analysis are the removal of telluric absorption features and Solar lines, the correction for systematics signatures (e.g., fringing), and the retrievals of the Mars atmospheric molecular abundances. Details on the first two components of the data analysis are found in our previously published work (Aoki et al., 2024).

To build a hemispheric map, we extracted multiple spectra along the slit for each slit position across the planet. The iSHELL slit dimension is 0.375″ × 15″and it has a plate scale of 0.125″/pixel in the wavelength direction and ∼0.165″/pixel (for Lp1-c) in the spatial direction (Rayner et al., 2012, 2022), thus covering about 3 × 90 pixels. To build a map, we extracted a spectrum from boxes of (3 × 3) pixels along the slit, covering about 0.375″ × 0.495″. The boxes are built by starting from the center of the slit defined as pixel number 0 and then grouping ±1 pixel in both directions. For each box, we extracted a spectrum and, after removing telluric absorption features and solar lines, performed retrievals using the PSG Optimal Estimation method included in the

21699100, 2025, 11, Downloaded from https://agupubs.onlinelibrary.wiley.com/doi/10.1029/2025JE009105 by Sara Faggi - Nasa Goddard , Wiley Online Library on [14/11/2025]. See the Terms and Conditions (https://onlinelibrary.wiley.com/terms-and-conditions) on Wiley Online Library for rules of use; OA articles are governed by the applicable Creative Commons License

21699100, 2025, 11, Downloaded from https://agupubs.onlinelibrary.wiley.com/doi/10.1029/2025JE009105 by Sara Faggi - Nasa Goddard , Wiley Online Library on [14/11/2025]. See the Terms and Conditions (https://onlinelibrary.wiley.com/terms-and-conditions) on Wiley Online Library for rules of use; OA articles are governed by the applicable Creative Commons License

astroPSG package. This allowed us to correct instrumental fringing and to further improve the frequency solution. The abundance values and 1-σ errors for H_2O and HCl were retrieved simultaneously from spectral order 152 of setting Lp1-c, while those for CO_2 were extracted from spectral order 142. We show an example of an extracted spectrum and retrieval in Figure 2b. The abundances of trace gases are derived with the PSG/OE retrieval package assuming temperature and pressure profiles from the Mars Climate Database 5.2 (MCD, (Millour et al., 2015)), and uniform vertical volume mixing ratios for HCl and H_2O. For clarity, water vapor and HCl abundances were retrieved from the main isotopic lines, assuming terrestrial isotopic ratios. The PSG RT calculations and retrievals can account for multiple scattering of dust and aerosols. However, as described by (Aoki et al., 2024), these effects were not included in our retrievals. Instead, we report HCl and H_2O column abundances relative to that of CO_2, deriving a CO_2 scaler that corrects for aerosol extinction along the line of sight. This scaler is derived from the CO_2 column density predicted by the MCD general circulation model and provides an estimate of the effective air mass. We then apply this scaler to the retrieved HCl and H_2O volume mixing ratios. It is important to note that the resulting HCl and H_2O abundances—corrected for aerosols and other opacity effects—correspond to the atmospheric abundances up to the altitudes where aerosols are not completely optically thick at these wavelengths.

Once obtained this set of values for all extracted spectra along the slit, and for all the slit positions across the Mars disk, we then created a map in the space of Δx [″] steps along the slit and Δy [″] shifts of the slit across the planet, using the center of the planet as a reference. The next step was then to convert this (Δx, Δy) map from arcseconds into projected latitude and longitude on Mars. The projected points would look as curved lines in the latitude/longitude coordinate frame due to the spherical projection, and as we collected the data over time and the planet rotates underneath, this effect further curves the slit positions. Lastly, we incorporated the effect of the astronomical seeing in the creation of the final maps. The information measured in the slit at a specific (Δx, Δy) position on the Martian disk, in reality, is the collection of the fluxes coming from the nearby regions within the seeing disk. The term seeing refers to the spatial smoothing (or degradation) of the information due to the distortion of the wavefronts of light as they pass through our atmosphere. Light encounters different temperature layers and different wind speeds, leading to an apparent displacement of the object over time due to variable refraction. These distortions vary at a high rate (∼milliseconds), and as we typically integrate over seconds or minutes, a point source becomes a blurred blob called "seeing disk" or simply "seeing." During our observing runs, we quantified the seeing effect (see Table 2), by measuring the spatial extent of a nearby star (point source) and fitting a Gaussian function, with the standard deviation (σ) and the FWHM of that Gaussian profile associated to the seeing as follows: seeing = FWHM = $2\sqrt{2}\,\sigma = 2.355*\sigma$. The seeing effect was specifically integrated into our analysis by creating a 2D Gaussian kernel image with a FWHM corresponding to the measured seeing during the observations. Therefore, the Mars maps, in the latitude/longitude coordinate frame, containing the retrieved abundance values for H_2O and HCl were first weighted to their 1-σ error and then spatially convolved to this 2D Gaussian kernel. This allowed us to account for fluxes of the planet measured away from the distinct physical boundaries of the slit that entered the slit. This means that the slit images would appear wider and smoothed than their physical size. Maps are shown in Figures 3, 6–8.

In Table 2, we report detailed information of our observing operations. The first column reports the date of the observation, while the second column reports the Mars angular diameter [″]. In the third column, we document the average value of the seeing during our observations. This parameter provides information about the actual angular resolution during our observations. As described above, astronomical observation quantifies the degradation of the telescope's diffraction-limited spatial resolution caused by atmospheric turbulence. The diffraction limit itself depends on the size of the telescope aperture. Seeing measurements also helped us define the most suitable step size for scanning across the Martian disk. On 18 May 2021 and 24 June 2021, we experienced poor (>1.5″) atmospheric seeing conditions, with measured values around 2.5–3″, which prevented us from mapping the planet. In these cases, the minimum achievable step size was comparable to half of the planet's angular diameter. The fourth column reports the number of slit positions used to map the planet. The fifth column shows the sampled surface area associated with each spectrum, extracted along the slit over a 3×3 pixel box, corresponding to $0.375'' \times 0.495''$. The sixth and seventh columns list the Central Meridional Longitude (CML) and the Mars Solar Longitude (L_S). A brief seasonal interpretation of the HCl behavior is given in the last column.

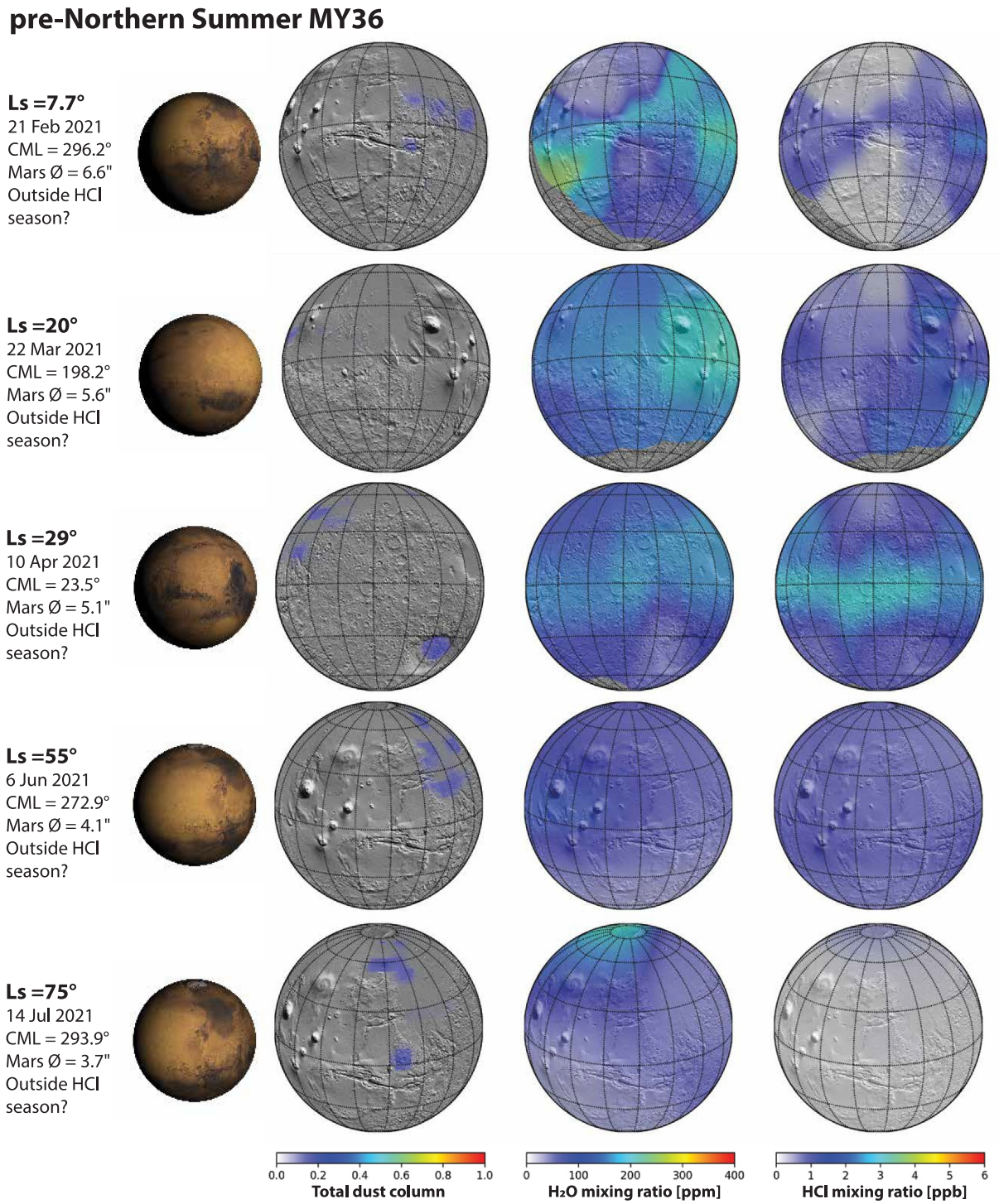

Figure 3. Global hemispheric maps for the first observing operations of 2021 during the pre-northern summer season in MY36. Each row, from left to right, presents key observational parameters: solar longitude (L_S [°]), observation date, central meridional longitude (CML [°]), Mars angular diameter (Ø [″]), and a brief note. These are followed by illumination conditions and three maps showing the total dust column optical depth (Montabone et al., 2015, 2020, 2024), the H_2O abundances ppm, and the Hydrogen chloride (HCl) abundances ppb measured by iSHELL/InfraRed Telescope Facility. All maps are normalized by the CO_2 scaler simultaneously measured in the same spectral setting. Equinoxes are typically dry, with some mid-latitudinal water vapor signature. No definitive strong activity of HCl is detected. In black and white, underneath the colored molecular abundance distributions, topography from the Mars Orbiter Laser Altimeter is shown (https://science.gsfc.nasa.gov/attic/mola/).

21699100, 2025, 11, Downloaded from https://agupubs.onlinelibrary.wiley.com/doi/10.1029/2025JE009105 by Sara Faggi - Nasa Goddard , Wiley Online Library on [14/11/2025]. See the Terms and Conditions (https://onlinelibrary.wiley.com/terms-and-conditions) on Wiley Online Library for rules of use; OA articles are governed by the applicable Creative Commons License

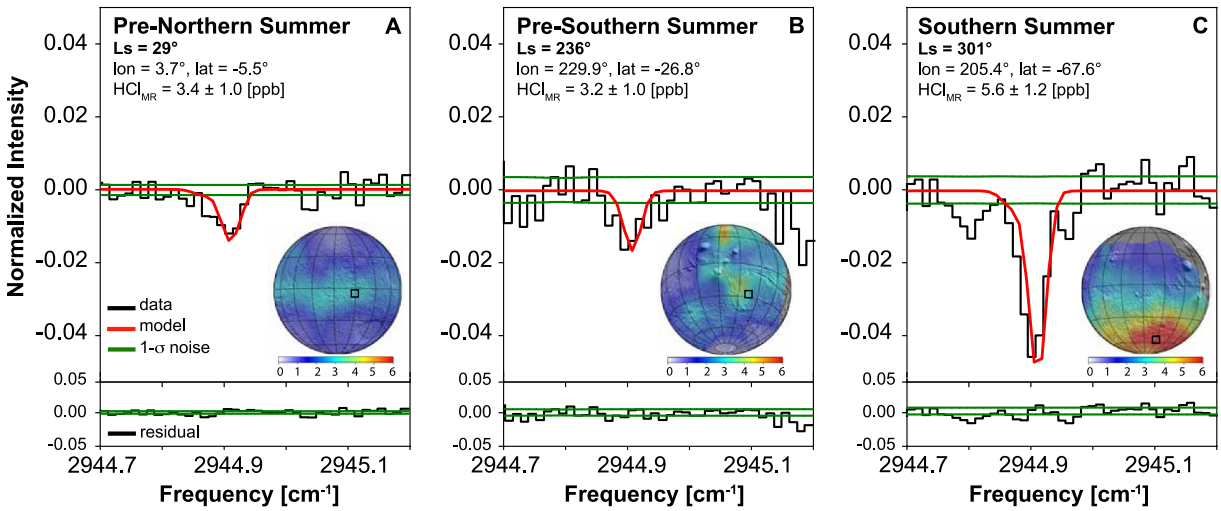

Figure 4. Examples of three Hydrogen chloride (HCl) detections: the pre-northern summer in Panel (a), the pre-southern summer in Panel (b), and the southern summer in Panel (c) For each season, we zoomed in on the HCl line at ∼2,945 cm^{-1}. The purpose of this plot is to show both the marginal (∼3σ) detections obtained at mid-latitudinal regions closer to the equinoxes (Panels a and b) and an example of the stronger detections obtained during the HCl season (Panel c). In each panel, the upper plot shows the Mars residual spectrum (black) after telluric subtraction and solar line removal. The model of HCl computed with PSG is shown in red superimposed on the data, and the final residual is displayed at the bottom. The noise envelope (±1σ) is shown in green. For each zoomed-in spectrum, the corresponding Martian map is shown, with a black box centered on the location from which the spectrum was extracted. Longitude and latitude are also provided for reference.

3. Results

Results from the two years of IRTF observations, covering most of the MY36 seasons, are presented in Figures 3, 6 and 7. Each row corresponds to an observing operation and provides, from left to right, information about the observing run, the Mars illumination conditions, and three maps. For each observation, we report the Solar Longitude (L_S) identifying the season, the MY, the date, the CML (or observer longitude), the Martian angular diameter and information related to the HCl season. This is followed by a colored image of Mars showing the planet's illumination conditions at the time of observation, which is crucial for properly accounting for the airmass and the viewing geometry in the RT scheme.

Three maps are then displayed. The first, based on data from (Montabone et al., 2015, 2020, 2024), shows the total atmospheric dust column optical depth (CDOD) centered at the CML at the time of observation (and same L_S), derived from measurements by the Mars Climate Sounder (MCS) on board of the Mars Reconnaissance Orbiter. It is important to note that these dust measurements were not used in the retrievals; they are included solely to illustrate the dust content during each observation and to only visually identify any possible correlation of HCl with dust. The middle and the right maps show our measured data and the retrieved water column and HCl column abundances relative to the retrieved CO_2 scaler. This ratio permits proper account for opacity along line of sight, as explained in the previous section (see Aoki et al., 2024 for more details).

The Mars maps will be presented and described below, grouped according to their respective Martian seasons. Further discussion on the potential sources and sinks will be provided in the following section.

3.1. Pre-Northern Summer Season

This first period of observations comprises five operations at L_S = 7.7°, 20°, 29°, 55°, and 75°, covering a time span from just after the Northern Spring Equinox (L_S ∼ 0°) to shortly before the beginning of the northern summer. Unfortunately, the latter season could not be observed due to unfavorable ground-based observing conditions. The primary goal of these observations was to explore the pre-summer season in the northern hemisphere, during which ExoMars/TGO did not detect HCl.

Equinoxes are usually characterized by water vapor mostly confined to the mid-low latitudes (within ±30°), while polar regions are generally dry. The Northern Spring Equinox (L_S = 0°) is typically drier than the Southern Spring Equinox (L_S = 180°) (M. D. Smith, 2002). During this period, as temperatures rise, a complex dynamical exchange occurs between surface ices in the northern polar reservoir and the subsequent atmospheric vapors

21699100, 2025, 11, Downloaded from https://agupubs.onlinelibrary.wiley.com/doi/10.1029/2025JE009105 by Sara Faggi - Nasa Goddard , Wiley Online Library on [14/11/2025]. See the Terms and Conditions (https://onlinelibrary.wiley.com/terms-and-conditions) on Wiley Online Library for rules of use; OA articles are governed by the applicable Creative Commons License

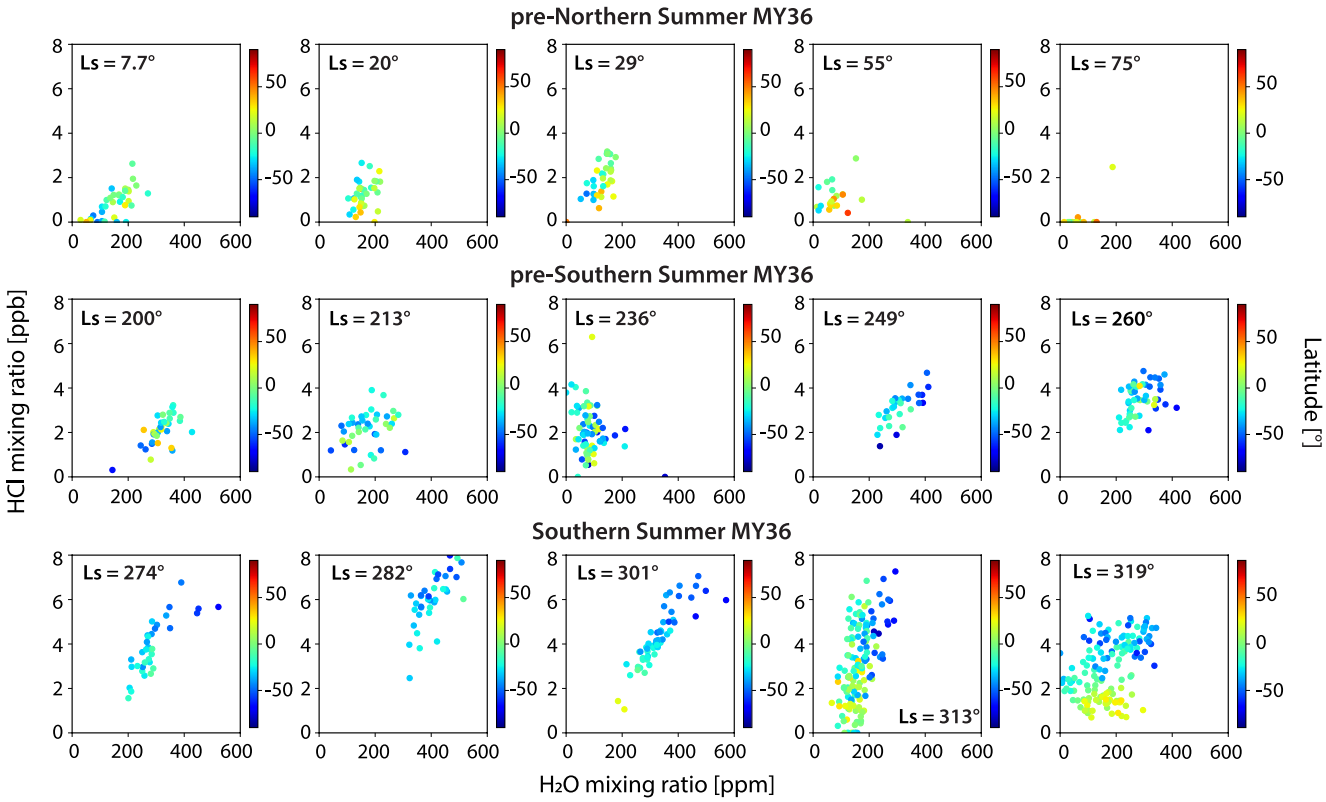

Figure 5. Water and Hydrogen chloride (HCl) correlation diagrams for the three seasons investigated across MY36. The *x*-axes show water mixing ratios [ppm], the *y*-axes show HCl mixing ratios [ppb], the colorbars indicate the latitudes [°] of the measurements.

(Montmessin et al., 2017; Montmessin et al., 2024). As the CO_2 seasonal frost starts to sublimate, it gradually unveils layers of the water ice cap. The deposits of seasonal water frost are mixed with freshly overlaid water ice grains dragged near the surface by the CO_2 ice sublimation. The redeposition of these water ice grains can consequently produce additional layers of water ice on top of the remaining seasonal CO_2 frost, leading to highly localized variations. The CO_2 polar frost generally disappears completely at $L_S \sim 80°$, just before the beginning of the northern summer, leaving the water ice cap exposed to sublimation. Immediately after $L_S \sim 90°$, the strongest water vapor abundances are observed in the northern atmosphere (Montmessin et al., 2017; Montmessin et al., 2024). Our maps, presented in Figure 3, capture the period preceding $L_S \sim 80°$, during the sublimation of the seasonal CO_2 frost and before the full exposure and sublimation of the underlying water ice cap. Our first operation at $L_S = 7.7°$ shows a possible lack of water vapor at northern high latitudes, indicating that water is likely still trapped in the North Polar Cap (NPC) in the form of ice.

Throughout the season, water vapor abundances are generally around 50–100 ppm or lower. Mid-to low-latitudinal (−30° to +30°) enhancements of up to 150–200 ppm are observed at $L_S = 7.7°$, 20° and $L_S = 29°$, probably due to the transport of water vapor toward the northern hemisphere via global circulation, following its sublimation from the southern pole near the perihelion. At $L_S = 75°$, we observe an initial enhancement of water vapor toward the NPC, indicating the onset of water ice sublimation.

During this pre-summer season in the northern hemisphere, we do not detect any definitive HCl signatures, in agreement with TGO measurements. HCl abundances—or upper limits—are around or below 1 ppb throughout the season. A local enhancement reaching 2–3 ppb around the equatorial latitudes (−15° to +15°) is seen at $L_S = 29°$ and appears to be correlated with a concurrent increase in water vapor at the same location. An example of HCl detection is reported in Figure 4a, while the correlation plot is shown in the top panels of Figure 5. It is important to highlight that the TGO solar measurements by ACS and NOMAD sample these Equatorial latitudes less frequently due to operational constraints; therefore, our measurements provide complementary coverage.

21699100, 2025, 11, Downloaded from https://agupubs.onlinelibrary.wiley.com/doi/10.1029/2025JE009105 by Sara Faggi - Nasa Goddard , Wiley Online Library on [14/11/2025]. See the Terms and Conditions (https://onlinelibrary.wiley.com/terms-and-conditions) on Wiley Online Library for rules of use; OA articles are governed by the applicable Creative Commons License

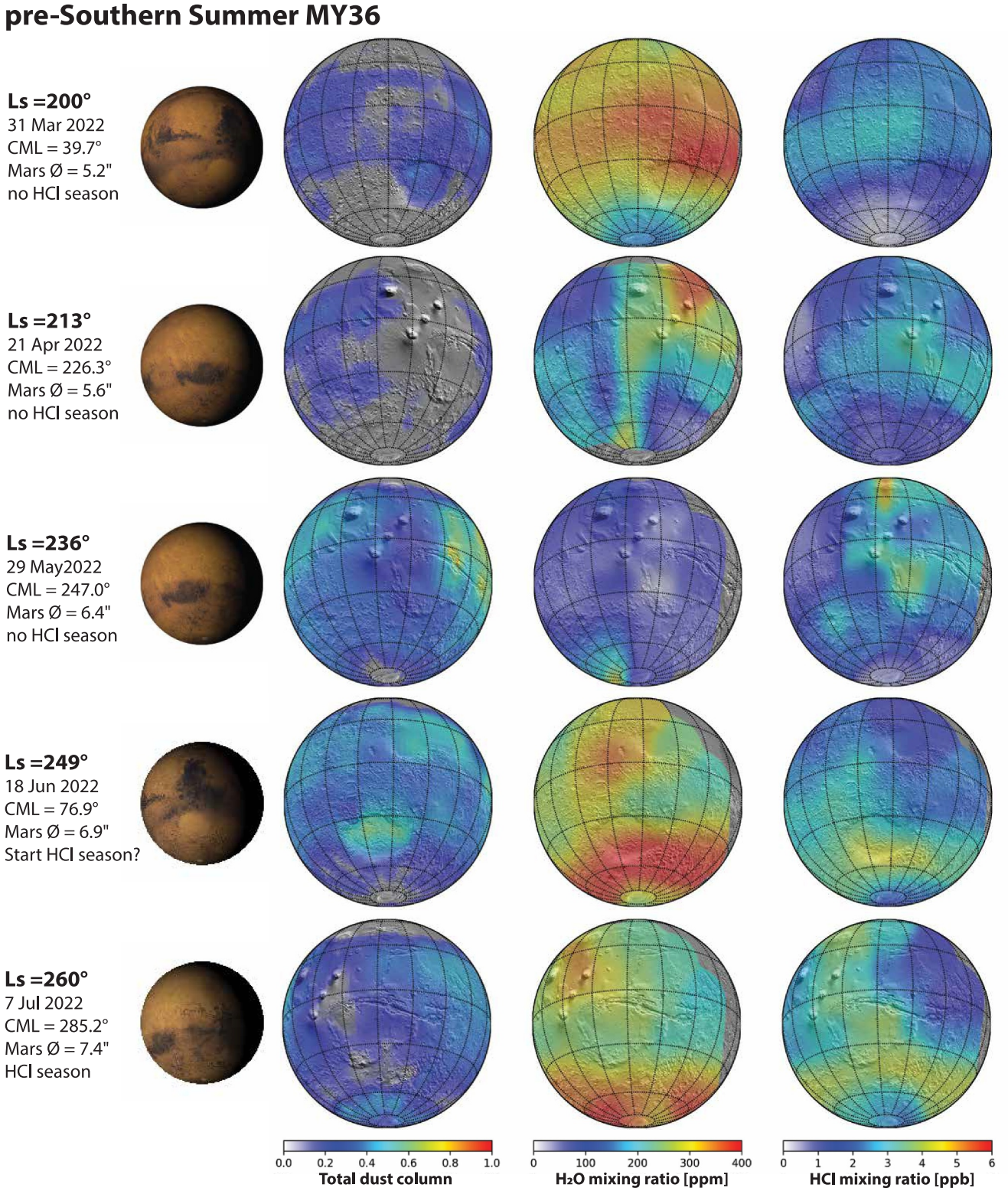

Figure 6.

21699100, 2025, 11, Downloaded from https://agupubs.onlinelibrary.wiley.com/doi/10.1029/2025JE009105 by Sara Faggi - Nasa Goddard , Wiley Online Library on [14/11/2025]. See the Terms and Conditions (https://onlinelibrary.wiley.com/terms-and-conditions) on Wiley Online Library for rules of use; OA articles are governed by the applicable Creative Commons License

21699100, 2025, 11, Downloaded from https://agupubs.onlinelibrary.wiley.com/doi/10.1029/2025JE009105 by Sara Faggi - Nasa Goddard , Wiley Online Library on [14/11/2025]. See the Terms and Conditions (https://onlinelibrary.wiley.com/terms-and-conditions) on Wiley Online Library for rules of use; OA articles are governed by the applicable Creative Commons License

These tentative detections could be explained by the potential release of HCl and water previously retained in high-altitude water ice clouds during the southern summer, which are subsequently transported from the southern to the northern hemisphere by the meridional circulation. The meridional circulation is generally dominated by Hadley cells (overturning flows) driven by the differential heating in the atmosphere. At Equinoxes, the circulation is characterized by two symmetric Hadley cells moving from the Equator toward the two Poles, driven by the rising air flow from the warm equatorial region. While Mars evolves from Equinoxes to the Solstices, the subsolar point shifts on the surface from the equatorial region toward the Poles. Therefore, the circulation evolves from two symmetric Hadley cells into a big primary Hadley cell that flows from one hemisphere to the other (e.g., from the North to the South at $L_S \sim 90°$ and vice versa at $L_S \sim 270°$) and a secondary small polar Hadley cell that is thermally driven. Since the pre-northern summer season is generally dust free, as shown in the maps extracted from the MCS database (Montabone et al., 2015, 2020), a speculative scenario is that water vapor could be released locally from the regolith or other minerals that previously adsorbed it into the surface, producing a surface-to-atmosphere exchange (Hu, 2019; Savijärvi et al., 2016; Steele et al., 2017). However, it is important to mention that the role of the regolith as efficient catalyzer has remained elusive. Many modeling efforts can reproduce the water cycle and the atmospheric variability without accounting for an exchange process between the surface and atmosphere outside the polar regions (Böttger et al., 2005; Montmessin et al., 2024).

3.2. Pre-Southern Summer Season

The southern polar region is considered another major reservoir of water ice, contributing to the seasonal water release into the Martian atmosphere. Patches of water ice are present both around the residual CO_2 ice cap and intermixed within the cap itself. Our second observation period specifically targeted the time preceding the southern summer ($L_S = 270°$), with the main objective of characterizing the beginning of the HCl season and its interplay with the onset of water sublimation from the South Pole and, if any, to identify a potential relationship with the presence of dust.

In the first half of 2022, we performed iSHELL observations at $L_S = 200°$, 213°, 236°, 249°, and 260°. The corresponding maps are shown in Figure 6. During the first observation, at $L_S = 200°$—close to the Southern Spring Equinox—we observed water vapor to be globally distributed at levels of about 250–300 ppm with an enhancement reaching 350 ppm between the equatorial and the southern mid-latitudes. As already mentioned, Equinoxes are characterized by the presence of water vapor at mid-to low latitudes, with the Southern Spring Equinox ($L_S = 180°$) being wetter than its northern counterpart. Within the same mid-latitudes (−30° to +30°), we again observed an enhancement also for HCl, with concentrations similar to those previously observed at $L_S = 29°$, during the pre-northern summer period. These tentative detections could be explained by Hadley circulation, which similarly transports water and HCl—probably previously trapped in water-ice clouds—from the Equator toward higher latitudes. In agreement with the hypothesis of its connection to the water cycle, HCl is absent near the South Pole during this season. A very tenuous dust column is also observed at similar latitudes.

The second observation run, at $L_S = 213°$, is still characterized by extended mid- to-low latitude distributions of both water and HCl, which appear to follow consistent spatial patterns. This time, dust appears to be mostly absent and does not exhibit the same behavior as the trace gases. The operations at $L_S = 213°$ and later at $L_S = 236°$ likely mark the beginning of southern water ice cap sublimation. While at $L_S = 236°$ water vapor is globally present at low abundances, a tenuous enhancement — reaching ∼200 ppm — is also observed toward southern polar latitudes in both operations. Strong HCl signatures remain absent in the South Polar region (see Figure 4b for illustration), and its spatial distribution still appears uncorrelated with that of water (see Figure 5). Some weak detections, at ∼3σ levels, are observed at mid-latitudes. These may represent a residual signature of meridional circulation, or alternatively, could hint at a distinct HCl production mechanism that is at least partially decoupled

Figure 6. Global hemispheric maps during the pre-southern summer season of MY36. Each row, from left to right, displays key observational parameters: solar longitude (L_S [°]), observation date, central meridional longitude (CML [°]), Mars angular diameter (∅ [″]), and a brief note. These are followed by illumination conditions and three maps showing the total dust column optical depth (Montabone et al., 2015, 2020, 2024), H_2O abundances ppm, and Hydrogen chloride (HCl) abundances ppb as measured by iSHELL/InfraRed Telescope Facility. These maps are normalized using the CO_2 scaler simultaneously derived from the same spectral setting. Between $L_S \sim 200°$ and 213°, an enhancement is observed at mid-latitudes, resulting from the meridional transport of water from the northern to the southern hemisphere. The onset of southern polar water ice cap sublimation is visible at $L_S \sim 236°$, while the beginning of the HCl season is identified around $L_S \sim 250°$. Black and white maps beneath the colored molecular abundance distributions show the Mars Orbiter Laser Altimeter topography (https://science.gsfc.nasa.gov/attic/mola/).

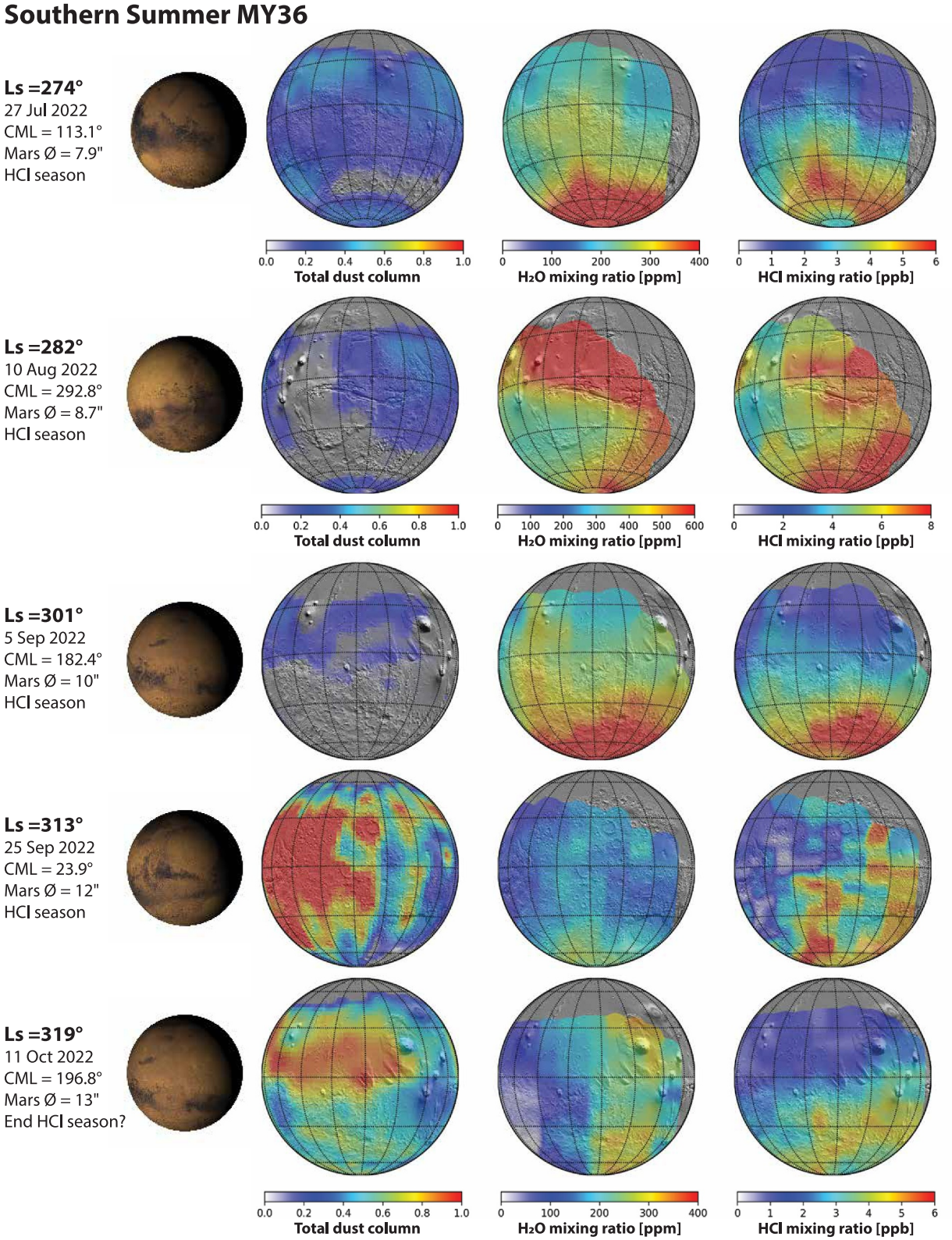

Figure 7.

21699100, 2025, 11, Downloaded from https://agupubs.onlinelibrary.wiley.com/doi/10.1029/2025JE009105 by Sara Faggi - Nasa Goddard , Wiley Online Library on [14/11/2025]. See the Terms and Conditions (https://onlinelibrary.wiley.com/terms-and-conditions) on Wiley Online Library for rules of use; OA articles are governed by the applicable Creative Commons License

21699100, 2025, 11, Downloaded from https://agupubs.onlinelibrary.wiley.com/doi/10.1029/2025JE009105 by Sara Faggi - Nasa Goddard , Wiley Online Library on [14/11/2025]. See the Terms and Conditions (https://onlinelibrary.wiley.com/terms-and-conditions) on Wiley Online Library for rules of use; OA articles are governed by the applicable Creative Commons License

from water vapor — possibly involving local dust uplifts. However, given the low signal-to-noise ratio of the HCl measurements, the apparent lack of correlation with water vapor at $L_S = 236°$ (see Figure 5) may simply reflect the challenges of the measurement, making it difficult to draw firm conclusions at this stage.

Finally, our last two observations during the pre-southern summer season, at $L_S = 249°$ and 260°, reveal a fully active south polar region. The water ice cap is now undergoing sublimation, with water column abundances reaching 250–400 ppm at southern high latitudes. HCl appears to follow the release of water vapor, with enhancements reaching ∼4–4.5 ppb in an annular pattern around the South Pole, indicating a correlation between the two species (see Figure 5). However, neither trace gas appears to be associated with dust. For example, the dust column peaks over Hellas Basin, whereas water and HCl abundances are enhanced along the southern edge of this basin. In addition, a patched mid-latitude distribution is observed for both water and HCl, but not for dust in the same region.

Based on these observations, we show that HCl abundances start to increase in the south around $L_S \sim 250°$ during MY36. This is largely consistent with previous TGO NOMAD and ACS measurements from MY34, MY35, and MY36 (Aoki et al., 2021; O. Korablev et al., 2021; Liuzzi et al., 2021; Olsen et al., 2021, 2024a; Trokhimovskiy et al., 2021). An example of spectrum observed at $L_S = 249°$ (on 18 June 2022), during the beginning of the HCl season, is shown in Figure 2b.

3.3. Southern Summer Season

The last season we investigated comprises five observing operations conducted at $L_S = 274°$, 282°, 301°, 313° and 319° (see Figure 7). These observations cover the southern summer season — during which HCl was originally discovered — to characterize the behavior of HCl at its maximum activity and identify its subsequent disappearance from the atmosphere. During this period, HCl is expected to peak at $L_S \sim 280°$ and to vanish by $L_S \sim 330°$.

As anticipated, our maps indeed show a significant enhancement in the HCl abundances at $L_S = 274°$ and 301°. In addition, notable extended spatial features are observed toward the end of the HCl season. When examining the water vapor and HCl maps from the first three operations ($L_S = 274°$, 282°, and 301°), we again find a strong spatial correlation between these species (see the last row of Figure 5) in contrast with the dust distribution (see Figure 7).

At $L_S = 274°$, the release of both water vapor and HCl is most pronounced toward the south polar regions, reaching about 350–400 ppm and 5–6 ppb, respectively. This pattern supports the idea of an HCl production process linked to the presence of water vapor, as proposed in previous studies (Aoki et al., 2021; O. Korablev et al., 2021; Olsen et al., 2021). Interestingly, HCl abundances are higher where dust columns are lower or nearly absent, and vice versa. This suggests that high dust loading is not strictly necessary for efficient HCl production and excessive dust may even contribute to HCl removal.

At $L_S = 282°$, along with the southern polar release of H_2O and HCl — reaching ∼500 ppm and 7–8 ppb, respectively — we observed a striking enhancement of water vapor at the Equatorial and mid-latitudes, with abundances of 500–600 ppm. This may be related to the presence of localized dust, which can raise atmospheric temperatures high enough to cause the sublimation of water ice clouds.

From the dust maps, we can see that the dust columns — with opacity values around 0.4–0.5 — are spatially distributed in regions similar to those where water vapor is present. HCl also shows enhanced abundances, reaching 6–8 ppb at similar mid-latitudes, suggesting a possible additional local source involving water and, to some extent, the presence of dust.

Figure 7. Global hemispheric maps covering the observing operations during the southern summer season in MY36. Each row, from left to right, displays key observational parameters: solar longitude (L_S [°]), date of the observations, central meridional longitude (CML [°]), Mars angular diameter (∅[″], and a brief note. These are followed by illumination conditions and three maps showing the total dust column optical depth (Montabone et al., 2015, 2020, 2024), the H_2O abundances ppm, and the Hydrogen chloride (HCl) abundances ppb measured by iSHELL/InfraRed Telescope Facility. These maps are normalized by the CO_2 scaler simultaneously measured in the same spectral setting. HCl reaches its peak activity from around $L_S \sim 274°$–301°. The end of the seasonal release is identified around $L_S \sim 319$. Black and white maps beneath the colored molecular abundance distributions show the Mars Orbiter Laser Altimeter topography (https://science.gsfc.nasa.gov/attic/mola/).

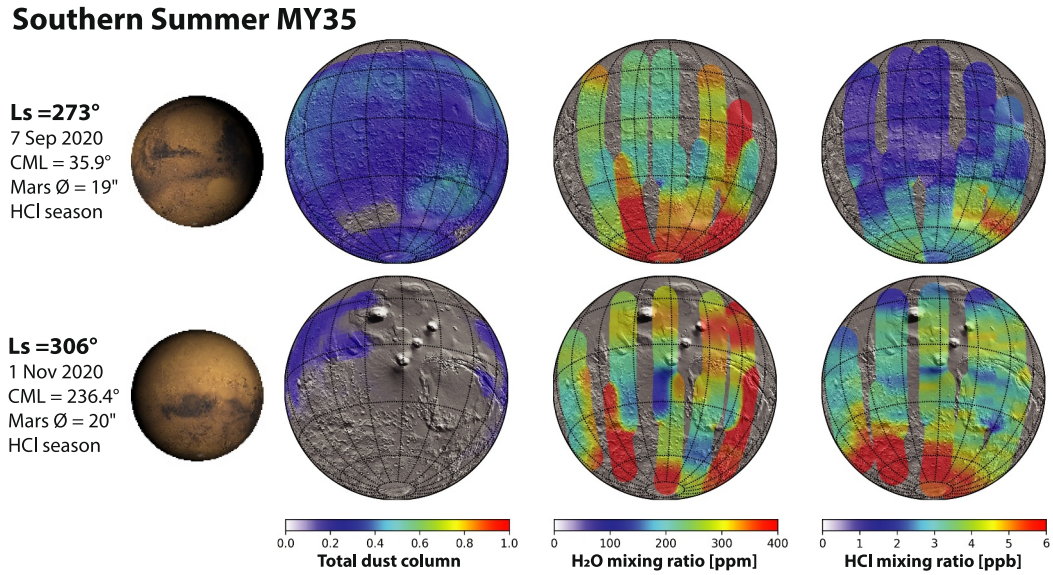

Figure 8. Global hemispheric maps covering the southern summer in MY35 and Director Discretionary Time in September and November of 2020 (Aoki et al., 2024). Each row, from left to right, displays key observational parameters: solar longitude (L_S [°]), date of the observations, central meridional longitude (CML [°]), Mars angular diameter (Ø[″]), and a brief note. Then, we show illumination conditions and three maps showing the total dust column optical depth (Montabone et al., 2015, 2020, 2024), the H_2O abundances [ppm], and the Hydrogen chloride abundances [ppb] measured by iSHELL/InfraRed Telescope Facility. These maps are normalized by the CO_2 scaler simultaneously measured in the same spectral setting. Black and white maps beneath the colored molecular abundance distributions show the Mars Orbiter Laser Altimeter topography (https://science.gsfc.nasa.gov/attic/mola/).

Contrary to what was observed at $L_S = 282°$, but similar to $L_S = 274°$, the observations at $L_S = 301°$ again show that the release of water vapor and HCl is maximized toward the southern polar regions. An example of HCl detection is shown in Figure 4c, while the water vapor-HCl correlation is displayed in the bottom panels of Figure 5. Notably, the HCl abundances measured at $L_S = 274°$ and $L_S = 301°$ agree with previous iSHELL observations during MY35 (Aoki et al., 2024). These earlier operations, performed as part of our DDT in September and November 2020, were part of our initial work to demonstrate the feasibility of ground-based observations and to confirm the HCl signature following its discovery by ExoMars/TGO. These first two

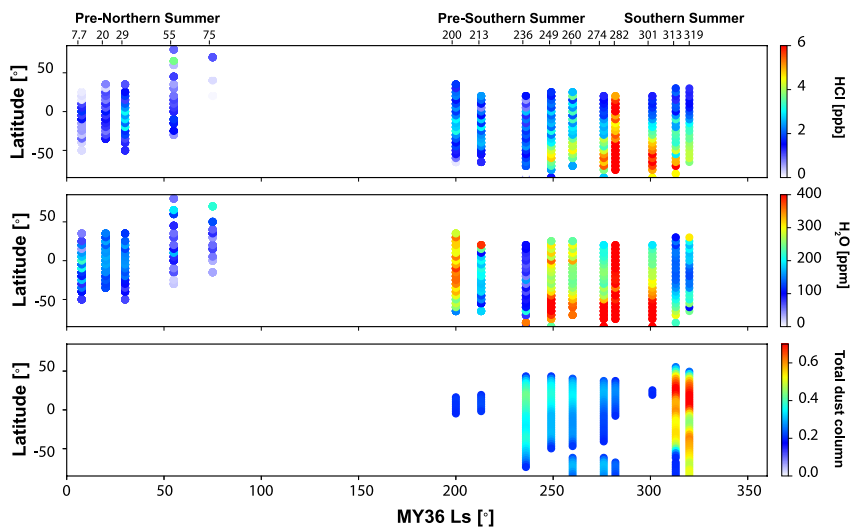

Figure 9. Longitudinally weighted mean of Hydrogen chloride [ppb] (top panel), water vapor [ppm] (middle panel), and total atmospheric dust column optical depth (CDOD) across MY36. The bottom x-axis shows the solar longitude L_S [°], while the top x-axis indicates the corresponding observed L_S seasons.

21699100, 2025, 11, Downloaded from https://agupubs.onlinelibrary.wiley.com/doi/10.1029/2025JE009105 by Sara Faggi - Nasa Goddard , Wiley Online Library on [14/11/2025]. See the Terms and Conditions (https://onlinelibrary.wiley.com/terms-and-conditions) on Wiley Online Library for rules of use; OA articles are governed by the applicable Creative Commons License

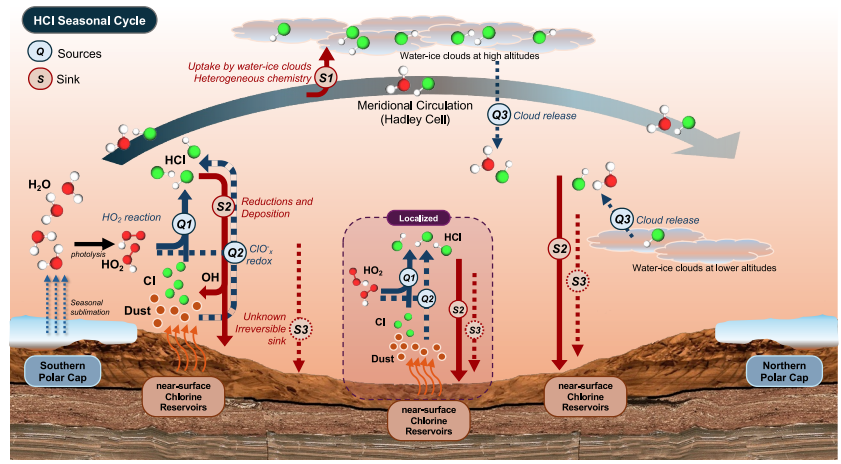

Figure 10. Schematic view of the Hydrogen chloride (HCl) seasonal cycle in the southern summer, updated from Figure 9 of Aoki et al. (2024). Possible processes contributing to the production (Q) and destruction (S) of HCl are illustrated. Q1 denotes the main HCl source mechanism, involving water photolysis products and chlorine radicals. Q2 refers to a redox-based production pathway involving dry perchlorates; its uncertain contribution is marked by a dotted line. Q3 represents a transient source related to the release of HCl from water ice clouds. S1 corresponds to the uptake onto water ice clouds at high altitudes, where heterogeneous chemistry might play a role. S2 represents the reaction with OH and, more generally, the deposition of chlorine species on the surface in the form of perchlorates. S3 represents a yet unidentified permanent sink process that effectively destroys HCl and allows it to redeposition on the surface; we highlighted its unclear nature with dotted lines. Note that the numbering of the sources and sinks does not identify their order of execution. In the schematic diagram, the primary Hadley cell, defining the hemispheric meridional circulation, is shown in blue.

observations in MY35 were instrumental in motivating our subsequent systematic observation campaign. They are reported in Figure 8 for completeness and for comparison with the same season in MY36, showing consistent HCl release patterns and suggesting a stable repeatable chlorine cycle in the Martian atmosphere.

Our last two operations — conducted at $L_S = 313°$ and 319° — appear to mark the end of the HCl seasonal cycle in the southern hemisphere and possibly the onset of Hadley cell meridional circulation toward the northern hemisphere. A marked reduction in water release is observed from the south pole, with values spanning 200–250 ppm. Water also starts exhibiting a more tenuous global distribution, reaching 100–150 ppm across mid- and equatorial latitudes. The HCl abundances similarly globally decline, with values reaching 4.5 ppb in the southern hemisphere.

Interestingly, at $L_S = 313°$, the HCl map reveals additional elongated spatial structures extending toward mid- and equatorial latitudes, with peaks reaching 5–6 ppb. The water vapor map shows a hint of similar spatial patterns, though less pronounced relative to its average global background. In the dust map, a storm is clearly identifiable near the Lunae Planum region (western longitudes) and toward the Arabia Terra, extending longitudinally over multiple latitudes, with high opacity values around 0.9–1. Conversely, dust in the eastern longitudes appears less optically thick but exhibits a longitudinal striped spatial distribution similar to that observed in the HCl map. This event is probably part of the annual "C" dust storm, which typically occurs around $L_S = 315°$ (Kass et al., 2016).

At $L_S = 313°$, a clear dichotomy can be observed between the spatial distributions of dust and HCl. In the Lunae Planum region (western longitudes), dust opacity is high, while HCl abundances are low (~1 ppb). In contrast, HCl shows enhanced abundances east of the CML, with peaks distributed along longitudinal stripes — resembling the dust pattern observed in the same region.

This behavior suggests that two distinct and potentially competing dust-related processes might influence both the production and removal of HCl. Part of this effect may be reflected in the steeper slope in the HCl–water vapor correlation at $L_S = 313°$ (see Figure 5), which could indicate the presence of an additional source of HCl. Alternatively, we may be observing the onset of meridional propagation of water vapor and HCl, and the role of dust in forming water ice clouds — removing both species from the atmosphere. Another possibility is that in regions with high dust loading, the presence of low-altitude dust may have prevented sensing the full atmospheric column. Interestingly, TGO measurements showed a decrease in HCl abundance immediately after the annual

21699100, 2025, 11, Downloaded from https://agupubs.onlinelibrary.wiley.com/doi/10.1029/2025JE009105 by Sara Faggi - Nasa Goddard , Wiley Online Library on [14/11/2025]. See the Terms and Conditions (https://onlinelibrary.wiley.com/terms-and-conditions) on Wiley Online Library for rules of use; OA articles are governed by the applicable Creative Commons License

21699100, 2025, 11, Downloaded from https://agupubs.onlinelibrary.wiley.com/doi/10.1029/2025JE009105 by Sara Faggi - Nasa Goddard , Wiley Online Library on [14/11/2025]. See the Terms and Conditions (https://onlinelibrary.wiley.com/terms-and-conditions) on Wiley Online Library for rules of use; OA articles are governed by the applicable Creative Commons License

"C" dust storm (Olsen et al., 2024a), suggesting that our observed HCl distribution during the storm — and the dependence on dust and water — might provide valuable insights into previously unexplored HCl sink processes.

In general, during the southern summer, the Martian atmosphere is warm enough to inhibit efficient water ice cloud formation, especially at lower altitudes. Therefore, the lack of clouds combined with strong perihelion circulation result in a rapid ascent of water vapor and HCl above ∼20 km, as well as their effective transport toward the winter hemisphere.

The formation of water ice clouds is known to critically depend on aerosols, which can either promote or suppress condensation. On Mars, water vapor condenses directly onto airborne dust particles to form ice crystals. This process requires specific conditions of water vapor saturation and is also influenced by dust grain size and concentration along with ambient pressure and temperature. Its efficiency varies with the vertical distribution of water in the atmosphere (Montmessin et al., 2024).

Our ground-based column integrated maps cannot provide information on the vertical distribution of dust layers or the location of the hygropause. Thus, we can only probe the horizontal presence or absence of trace gases and compare them spatially with the dust distributions measured by MCS. However, only vertical profiles are needed to understand how these gases are influenced by dust.

Our last observing operation at $L_S = 319°$ again shows a behavior similar to that observed at $L_S = 274°$ and 301°. The release of water vapor and HCl now appears to originate primarily from the southern region and at relatively low concentrations, as expected near the end of their seasonal cycles.

While water vapor extends toward equatorial latitudes — possibly reflecting transport by the global circulation — HCl does not show a similar spatial distribution. This may also be reflected in the correlation plot in Figure 5, where two distinct trends are observed: one indicating the correlation between water vapor and HCl and a second one with a shallower slope. This difference might be explained by the potential uptake of HCl by water ice clouds forming at high altitudes. However, we cannot exclude that other interpretations can explain these distinct trends observed in Figure 5. For example, another explanation could be that the correlation between HCl and water vapor observed earlier start disappearing at the end of the seasonal cycle of HCl.

Interestingly, in regions where dust opacity is higher—such as over Amazonis Planitia —HCl abundances are again lower with values around 1 ppb.

4. Discussion

Decades of observations of the Martian atmosphere—from Earth, orbiters, and in situ missions— have shown that Mars' climate generally follows globally repeatable seasonal patterns, occasionally disrupted by variable dust events. It is widely accepted that the MY can be divided into two main climate periods: a warmer season near the southern summer, when Mars is at perihelion and conditions are typically dusty; and a cooler season near the northern summer, when Mars is at aphelion and characterized by low-latitude water ice clouds and generally dust-free conditions.

The Martian water cycle is arguably the best-studied seasonal pattern. The polar water ice caps start sublimating around $L_S \sim 80°$ in the northern hemisphere and around $L_S \sim 250°$ in the southern hemisphere, leading to high abundances of water vapor over the respective polar regions during each hemisphere's summer. Dust storms — whether globally or locally — can dramatically alter atmospheric temperatures through multiple scattering by dust grains, affecting both atmospheric circulation and water condensation. These effects can result in significant interannual climatological variability.

By following Mars over three seasons in MY36, we investigated both repeatable and unique features that characterize the HCl season and its relationship with the well-known water cycle. We confirmed the timing of the HCl cycle, and studied the spatial distributions of water vapor and HCl to explore potential source and sink processes.

Figure 9 shows the longitudinally average behavior of HCl, water vapor, and dust across the MY36, while Figure 10 summarizes the main processes potentially involved in the production and removal of HCl to the best of our knowledge. Below, we describe these processes and discuss how they may be identified in the data presented in Figures 3 and 5–7.

21699100, 2025, 11, Downloaded from https://agupubs.onlinelibrary.wiley.com/doi/10.1029/2025JE009105 by Sara Faggi - Nasa Goddard , Wiley Online Library on [14/11/2025]. See the Terms and Conditions (https://onlinelibrary.wiley.com/terms-and-conditions) on Wiley Online Library for rules of use; OA articles are governed by the applicable Creative Commons License

4.1. Sources

The main HCl production mechanism in the Martian atmosphere, labeled as Q1 in Figure 10, involves both water vapor photolysis products and chlorine (Cl) radicals. The beginning of the HCl cycle occurs around the start of the southern summer season. As the polar water frost begins to sublimate, water vapor is released into the atmosphere and photodissociated by solar UV radiation, producing species such as hydroperoxyl (HO_2), hydrogen peroxide (H_2O_2), and molecular hydrogen (H_2). Simultaneously, dust particles containing chloride-bearing compounds — such as chlorine salts including NaCl, KCl, and $FeCl_3$ — are also lifted into the atmosphere. These particles may release reactive chlorine species through UV irradiation or possibly electrostatic discharge (Laube et al., 2010; Wang et al., 2020). These reactive radicals can rapidly form HCl via gas-phase reactions. Under Martian atmospheric conditions, the dominant pathway is believed to be (Lefèvre & Krasnopolsky, 2017; M. L. Smith et al., 2014; Wilson et al., 2016):

$$HO_2 + Cl \rightarrow HCl + O_2$$

A second potential production pathway for HCl, labeled as Q2 in Figure 10, may involve redox chemistry between dust and photochemical byproducts of water vapor. A possible mechanism following this pathway was discussed by (O. Korablev et al., 2021), based on an earlier work by (Catling et al., 2010, 2013), suggesting that nitrates present on airborne dust promote the production of highly reactive acids such as nitric acid (HNO_3) or peroxynitric acid (HNO_4). These acids could then oxidize dry perchlorates (ClO_4^-) releasing molecular chlorine (Cl_2), which would photodissociate into chlorine radicals. These radicals would subsequently react with water vapor photochemical products to form HCl. However, this mechanism is known to be efficient on Earth only in the presence of liquid water, and its efficiency under Mars conditions remains uncertain. The contribution of this Q2 pathway to atmospheric HCl production is therefore still unclear.

At $L_S \sim 249°$, our data suggest that Q1 is probably the dominant pathway initiating the HCl cycle during the pre-summer season in the southern hemisphere. At this time, the maps of water vapor and HCl show significant release confined to an annular region surrounding the South Pole. This might be explained by the sublimation of CO_2 frost, which starts to uncover an annulus of underlying water ice that subsequently sublimates. These two production mechanisms may continue to operate throughout the southern summer, as supported by the strong spatial correlation between the distributions of water and HCl.

An additional transient source process for HCl, labeled as Q3 in Figure 10, could be related to its release from water ice cloud particles. While uptake by these particles is considered a potential sink mechanism (discussed in the next section), a partial re-release may also occur. As HCl is transported to high altitudes along with water, it may adsorb onto ice particles through initial deposition followed by condensation. When atmospheric circulation subsequently transports the ice cloud particles to lower altitudes and mid-latitudes in the northern hemisphere, part of the HCl could be released back into the atmosphere. This process might explain the enhancements of HCl observed, for example, at $L_S \sim 29°$ during the pre-northern summer or at $L_S \sim 200°$, 213°, and 236° during the pre-southern summer season.

Together with the seasonally repeatable production of HCl from the southern polar region (the northern counterpart has not yet been explored in detail), we also identify spatially localized source regions that are most likely characterized by the same production mechanism, Q1. These localized sources are observed at $L_S \sim 249°$ and 260° in equatorial and northern mid-latitudes, where enhanced water vapor coincides with low dust columns, further demonstrating the role of water photolysis products in HCl production. Similar local enhancements are also seen at $L_S \sim 282°$ and 313°, spanning both southern and northern mid-latitudes, and are now correlated with both the presence of water vapor and dust.

Dust plays a key role in modifying atmospheric conditions: by absorbing and scattering incoming solar radiation, it warms the atmosphere (e.g., Madeleine et al., 2011; Pollack et al., 1979; Smith et al., 2001), which can reduce water ice cloud formation and potentially favor HCl production. However, we also observe an anticorrelation between HCl and high dust columns, suggesting that excessive dust could contribute to HCl removal or inhibit its formation.

21699100, 2025, 11, Downloaded from https://agupubs.onlinelibrary.wiley.com/doi/10.1029/2025JE009105 by Sara Faggi - Nasa Goddard , Wiley Online Library on [14/11/2025]. See the Terms and Conditions (https://onlinelibrary.wiley.com/terms-and-conditions) on Wiley Online Library for rules of use; OA articles are governed by the applicable Creative Commons License

4.2. Sinks

Previous orbital measurements suggested that HCl is abundant below the hygropause (e.g., Luginin et al., 2024). As discussed in Aoki et al. (2021) and Liuzzi et al. (2021), there are a few mechanisms that, in principle, could efficiently deplete HCl in the middle atmosphere. We summarize these below, along with references to the seasons during which they may have been observed.

The first sink mechanism for HCl — labeled as S1 in Figure 10 — is its uptake by water ice clouds. As discussed in previous studies, HCl and H_2O exhibit similar vertical distributions, suggesting that HCl is transported alongside H_2O and can become trapped within growing water ice particles (Kippenberger et al., 2019). The formation of these clouds depends on the presence and size of dust nuclei, and is often triggered by regional dust storms. Water ice clouds usually start appearing at midlatitudes in the southern hemisphere — a behavior observed by TGO during the perihelion season of MY34 (Liuzzi et al., 2020). In our data set, based on column-integrated abundances, we cannot directly detect the presence of water ice clouds. However, we can speculate on their potential occurrence at $L_S \sim 313°$, where we observe coincident high dust columns (e.g., over the Lunae Planum), reduced water abundances, and an almost complete absence of HCl.

As part of the uptake process by water ice clouds, it has been proposed that heterogeneous chemistry on the surface of water ice particles might contribute to the destruction of HCl (McKeachie et al., 2004; Rajendran et al., 2025; Streeter et al., 2025; Taysum et al., 2024b). A fraction of the HCl adsorbed onto ice surfaces could be oxidized leading to the formation of reactive chlorine-bearing species such as $ClONO_2$, HOCl, $ClNO_2$, or even Cl_2. Once released in the atmosphere, these compounds may be involved in the formation of perchloric acid ($HClO_4$), which could then be deposited onto the surface and subsequently converted into perchlorate salts (Catling et al., 2010; M. L. Smith et al., 2014; S. Solomon, 1999; Wilson et al., 2016). However, the lifetime of these intermediates, their high reactivity, the efficiency of heterogeneous pathways, and the influence of dust are competing factors that are not yet fully understood in the HCl cycle.

Another sink mechanism, labeled as S2 in Figure 10, could be through its chemical reaction with OH:

$$OH + HCl \rightarrow Cl + H_2O.$$

The products of water photolysis are essential to produce HCl, so OH represents a competing species, meaning that water can act both as a driver for HCl and, to some extent, as a sink (Michelsen et al., 1996). It is important to consider that this process is nevertheless much slower than the production process (see discussion in Aoki et al., 2021).

A permanent sink of HCl on the short timescales, labeled as S3 in Figure 10, remains puzzling. Although several possible sources and sinks have already been discussed in this study and in previous works (Aoki et al., 2021, 2024; O. Korablev et al., 2021; Liuzzi et al., 2021; Olsen et al., 2021), an open question still remains: how is HCl removed from the atmosphere? The lifetime of HCl (90 Sols below 15 km, see Aoki et al., 2021) appears inconsistent with this, suggesting the existence of an additional, faster chemical pathway or a process perhaps linked to high dust columns, which efficiently facilitate HCl destruction and its deposition on the surface as perchlorates.

5. Conclusions

In this work, we presented a methodic investigation of the Martian atmosphere targeting HCl and water using the high-resolution echelle spectrograph, iSHELL, at the NASA IRTF observatory. We systematically explored three Martian seasons in MY36, investigating the HCl cycle and analyzing its spatial distributions to study its relationship with water vapor and dust. Below, we summarize our key findings.

- During the pre-northern summer season, we explored the Martian atmosphere from $L_S \sim 7.7°$–$75°$ with five observing operations. No definitive HCl signatures were detected in agreement with TGO measurements. HCl abundances — or upper limits — remain around or below 1 ppb throughout the season. A possible enhancement at equatorial latitudes is observed at $L_S = 29°$, reaching 2–3 ppb, and appears to be correlated with a water vapor enhancement at similar locations. We interpreted this as the possible release of HCl and water vapor previously retained in high-altitude water ice clouds and transported meridionally from the southern to the northern hemisphere.

21699100, 2025, 11, Downloaded from https://agupubs.onlinelibrary.wiley.com/doi/10.1029/2025JE009105 by Sara Faggi - Nasa Goddard , Wiley Online Library on [14/11/2025]. See the Terms and Conditions (https://onlinelibrary.wiley.com/terms-and-conditions) on Wiley Online Library for rules of use; OA articles are governed by the applicable Creative Commons License

- During the pre-southern summer season, Mars was observed at five distinct times between $L_S = 200°$ and 260°. At $L_S = 200°$, water vapor was relatively abundant at mid-latitudes and depleted in the polar regions, as expected around the equinox. A possible enhancement in HCl abundance was observed at mid-latitudes as well. This feature could again be explained by the meridional circulation transporting both water vapor and HCl released from the sublimation of water ice clouds. Subsequent observations confirmed that the HCl seasonal cycle begins around $L_S = 250°$. The global-scale spatial distributions of both gas species were analyzed in an effort to identify potential source and sink processes for HCl. We confirmed that the seasonal increase in HCl abundance starts over the southern polar region, following the onset of water ice cap sublimation from that area. A localized HCl enhancement is also observed in association with the presence of dust. This could reflect a release of HCl triggered by the interplay between dust and water vapor at localized areas.
- The southern summer season was explored through five observing operations between $L_S \sim 274°$ and 319°. Our maps show the peak HCl activity between $L_S = 274°$ and 301°, consistent with TGO observations (Aoki et al., 2021; O. Korablev et al., 2021; Olsen et al., 2021). The end of its seasonal cycle is identified around $L_S = 313°–319°$. Our observations also confirm a strong correlation between the spatial distributions of water vapor and HCl, indicating that water vapor plays an important role in HCl production as proposed in previous studies. The role of dust appears more complex, suggesting the coexistence of two competing processes — one enhancing HCl production and the other promoting its destruction. As in the previous season, we again observed HCl enhancement at mid-latitudes, possibly driven by the interplay between dust and water vapor.

Conflict of Interest

The authors declare no conflicts of interest relevant to this study.

Data Availability Statement

The raw data used in this manuscript are publicly available at the NASA/IRTF archive (https://irtfweb.ifa.hawaii.edu/research/irtf_data_archive.php), and they can be downloaded by searching for the following observing program IDs: 2020B94, 2021A069, 2022A028, 2022B019.

The retrieval software package used in this study was the Planetary Spectrum Generator (PSG) (Villanueva et al., 2018), which is free and available online at https://psg.gsfc.nasa.gov. The data-reduction scripts are available at https://github.com/nasapsg. Figures were made with Matplotlib v.3.2.1, which is available under the Matplotlib license at https://matplotlib.org/.

The data products are text files (.txt) containing the retrieved abundances of water and HCl across the Marian disk. These numerical data, underpinning Figures 3–9, are stored and publicly available in Faggi et al. (2025).

Acknowledgments

Data presented in this work were obtained at the NASA-Infrared Telescope Facility, operated by the University of Hawai'i. We profoundly thank the staff of IRTF for their outstanding operational skills and valuable technical support during the 2 years of the observing campaign. The authors wish to recognize and acknowledge the very significant cultural role and reverence that the summit of Maunakea has always had within the indigenous Hawaiian community. We are most fortunate to have the opportunity to conduct observations from this mountain. For this work, SF and GLV were supported by NASA's Mars Program Office under "Participation in the TGO/NOMAD Investigation of Trace Gases on Mars". SA is supported by JSPS KAKENHI Grants 24K21565, 22K03709, 22H05151, 22H00164, and 22KK0044.

References

Aoki, S., Daerden, F., Viscardy, S., Thomas, I. R., Erwin, J. T., Robert, S., et al. (2021). Annual appearance of hydrogen chloride on Mars and a striking similarity with the water vapor vertical distribution observed by TGO/NOMAD. *Geophysical Research Letters*, *48*(11), e92506. https://doi.org/10.1029/2021GL092506

Aoki, S., Faggi, S., Villanueva, G. L., Liuzzi, G., Sagawa, H., Daerden, F., et al. (2024). Global mapping of HCl on Mars by IRTF/iSHELL. *The Planetary Science Journal*, *5*(7), 158. https://doi.org/10.3847/PSJ/ad58dc

Aoki, S., Vandaele, A. C., Daerden, F., Villanueva, G. L., Liuzzi, G., Clancy, R. T., et al. (2022). Global vertical distribution of water vapor on Mars: Results from 3.5 years of ExoMars-TGO/NOMAD science operations. *Journal of Geophysical Research: Planets*, *127*(9), e2022JE007231. https://doi.org/10.1029/2022JE007231

Böttger, H. M., Lewis, S. R., Read, P. L., & Forget, F. (2005). The effects of the Martian regolith on GCM water cycle simulations. *Icarus*, *177*(1), 174–189. https://doi.org/10.1016/j.icarus.2005.02.024

Braude, A. S., Montmessin, F., Olsen, K. S., Trokhimovskiy, A., Korablev, O. I., Lefèvre, F., et al. (2022). No detection of SO2, H2S, or OCS in the atmosphere of Mars from the first two martian years of observations from TGO/ACS. *Astronomy and Astrophysics*, *658*, A86. https://doi.org/10.1051/0004-6361/202142390

Catling, D. C., Claire, M. W., Zahnle, K. J., Quinn, R. C., Clark, B. C., Hecht, M. H., & Kounaves, S. (2010). Atmospheric origins of perchlorate on Mars and in the Atacama. *Journal of Geophysical Research*, *115*(E1). https://doi.org/10.1029/2009JE003425

Catling, D. C., & Moore, J. M. (2003). The nature of coarse-grained crystalline hematite and its implications for the early environment of Mars. *Icarus*, *165*(2), 277–300. https://doi.org/10.1016/S0019-1035(03)00173-8

Catling, D. C., Smith, M. L., Claire, M. W., & Zahnle, K. J. (2013). *Atmospheric chemistry of nitrogen on Mars: A link between oxidants in the soil and chlorine cycling*. European Planetary Science Congress.

Crismani, M. M. J., Villanueva, G. L., Liuzzi, G., Smith, M. D., Knutsen, E. W., Daerden, F., et al. (2021). A global and seasonal perspective of Martian water vapor from ExoMars/NOMAD. *Journal of Geophysical Research: Planets*, *126*(11), e2021JE006878. https://doi.org/10.1029/2021JE006878

Daerden, F., Neary, L., Villanueva, G., Liuzzi, G., Aoki, S., Clancy, R. T., et al. (2022). Explaining NOMAD D/H observations by cloud-induced fractionation of water vapor on Mars. *Journal of Geophysical Research: Planets*, *127*(2), e2021JE007079. https://doi.org/10.1029/2021JE007079

DiSanti, M. A., Bonev, B. P., Magee-Sauer, K., Russo, N. D., Mumma, M. J., Reuter, D. C., & Villanueva, G. L. (2006). Detection of formaldehyde emission in Comet C/2002 T7 (LINEAR) at infrared wavelengths: line-by-line validation of modeled fluorescent intensities. *The Astrophysical Journal*, *650*(1), 470–483. https://doi.org/10.1086/507118

Encrenaz, T., Bézard, B., Greathouse, T. K., Richter, M. J., Lacy, J. H., Atreya, S. K., et al. (2004). Hydrogen peroxide on Mars: Evidence for spatial and seasonal variations. *Icarus*, *170*(2), 424–429. https://doi.org/10.1016/j.icarus.2004.05.008

Encrenaz, T., Greathouse, T. K., Aoki, S., Daerden, F., Giuranna, M., Forget, F., et al. (2019). Ground-based infrared mapping of H2O2 on Mars near opposition. *Astronomy and Astrophysics*, *627*, A60. https://doi.org/10.1051/0004-6361/201935300

Faggi, S., Shohei, A., Liuzzi, G., Villanueva, G., Sagawa, H., Mumma, M., et al. (2025). Maps of HCl and H2O abundances in the Martian atmosphere in MY36 [Dataset]. *Zenodo*. https://doi.org/10.5281/zenodo.17209612

Fedorova, A., Montmessin, F., Trokhimovskiy, A., Luginin, M., Korablev, O., Alday, J., et al. (2023). A two-Martian Years survey of the water vapor saturation state on Mars based on ACS NIR/TGO occultations. *Journal of Geophysical Research: Planets*, *128*(1), e2022JE007348. https://doi.org/10.1029/2022JE007348

Fedorova, A. A., Montmessin, F., Korablev, O., Luginin, M., Trokhimovskiy, A., Belyaev, D. A., et al. (2020). Stormy water on Mars: The distribution and saturation of atmospheric water during the dusty season. *Science*, *367*(6475), 297–300. https://doi.org/10.1126/science.aay9522

Gaillard, F., & Scaillet, B. (2009). The sulfur content of volcanic gases on Mars. *Earth and Planetary Science Letters*, *279*(1), 34–43. https://doi.org/10.1016/j.epsl.2008.12.028

Glavin, D. P., Freissinet, C., Miller, K. E., Eigenbrode, J. L., Brunner, A. E., Buch, A., et al. (2013). Evidence for perchlorates and the origin of chlorinated hydrocarbons detected by SAM at the Rocknest aeolian deposit in gale crater. *Journal of Geophysical Research: Planets*, *118*(10), 1955–1973. https://doi.org/10.1002/jgre.20144

Hartogh, P., Jarchow, C., Lellouch, E., Val-Borro, M. de, Rengel, M., Moreno, R., et al. (2010). Herschel/HIFI observations of Mars: First detection of O2 at submillimetre wavelengths and upper limits on HCl and H2O2. *Astronomy and Astrophysics*, *521*, L49. https://doi.org/10.1051/0004-6361/201015160

Hecht, M. H., Kounaves, S. P., Quinn, R. C., West, S. J., Young, S. M. M., Ming, D. W., et al. (2009). Detection of perchlorate and the soluble chemistry of martian soil at the Phoenix lander site. *Science*, *325*(5936), 64–67. https://doi.org/10.1126/science.1172466

Hu, R. (2019). Predicted diurnal variation of the deuterium to hydrogen ratio in water at the surface of Mars caused by mass exchange with the regolith. *Earth and Planetary Science Letters*, *519*, 192–201. https://doi.org/10.1016/j.epsl.2019.05.017

Kass, D. M., Kleinböhl, A., McCleese, D. J., Schofield, J. T., & Smith, M. D. (2016). Interannual similarity in the Martian atmosphere during the dust storm season. *Geophysical Research Letters*, *43*(12), 6111–6118. https://doi.org/10.1002/2016GL068978

Khayat, A. S., Villanueva, G. L., Mumma, M. J., & Tokunaga, A. T. (2015). A search for SO2, H2S and SO above Tharsis and Syrtis volcanic districts on Mars using ground-based high-resolution submillimeter spectroscopy. *Icarus*, *253*, 130–141. https://doi.org/10.1016/j.icarus.2015.02.028

Kippenberger, M., Schuster, G., Lelieveld, J., & Crowley, J. N. (2019). Trapping of HCl and oxidised organic trace gases in growing ice at temperatures relevant to cirrus clouds. *Atmospheric Chemistry and Physics*, *19*(18), 11939–11951. https://doi.org/10.5194/acp-19-11939-2019

Korablev, O., Olsen, K. S., Trokhimovskiy, A., Lefèvre, F., Montmessin, F., Fedorova, A. A., et al. (2021). Transient HCl in the atmosphere of Mars. *Science Advances*, *7*(7), eabe4386. https://doi.org/10.1126/sciadv.abe4386

Korablev, O., Vandaele, A. C., Montmessin, F., Fedorova, A. A., Trokhimovskiy, A., Forget, F., et al. (2019). No detection of methane on Mars from early ExoMars Trace gas orbiter observations. *Nature*, *568*(7753), 517–520. https://doi.org/10.1038/s41586-019-1096-4

Korablev, O. I., Bertaux, J.-L., & Dubois, J.-P. (2001). Occultation of stars in the UV: Study of the atmosphere of Mars. *Journal of Geophysical Research*, *106*(E4), 7597–7610. https://doi.org/10.1029/2000JE001298

Kounaves, S. P., Hecht, M. H., Kapit, J., Quinn, R. C., Catling, D. C., Clark, B. C., et al. (2010). Soluble sulfate in the martian soil at the Phoenix landing site. *Geophysical Research Letters*, *37*(9). https://doi.org/10.1029/2010GL042613

Krasnopolsky, V., & Lefèvre, F. (2013). Chemistry of the Atmospheres of Mars, Venus, and Titan. https://doi.org/10.2458/azu_uapress_9780816530595-ch11

Krasnopolsky, V. A. (2022). Photochemistry of HCl in the martian atmosphere. *Icarus*, *374*, 114807. https://doi.org/10.1016/j.icarus.2021.114807

Krasnopolsky, V. A., Bjoraker, G. L., Mumma, M. J., & Jennings, D. E. (1997). High-resolution spectroscopy of Mars at 3.7 and 8 μm: A sensitive search for H2O2, H2CO, HCl, and CH4, and detection of HDO. *Journal of Geophysical Research*, *102*(E3), 6525–6534. https://doi.org/10.1029/96JE03766

Laube, J. C., Kaiser, J., Sturges, W. T., Bönisch, H., & Engel, A. (2010). Chlorine isotope fractionation in the stratosphere. *Science*, *329*(5996), 1167. https://doi.org/10.1126/science.1191809

Lefèvre, F., & Krasnopolsky, V. (2017). Atmospheric photochemistry. In F. Forget, M. D. Smith, R. T. Clancy, R. W. Zurek, & R. M. Haberle (Eds.), *The atmosphere and climate of Mars* (pp. 405–432). Cambridge University Press. https://doi.org/10.1017/9781139060172.013

Liuzzi, G., Villanueva, G. L., Crismani, M. M. J., Smith, M. D., Mumma, M. J., Daerden, F., et al. (2020). Strong variability of Martian water ice clouds during dust storms revealed from ExoMars trace gas Orbiter/NOMAD. *Journal of Geophysical Research: Planets*, *125*(4), e2019JE006250. https://doi.org/10.1029/2019JE006250

Liuzzi, G., Villanueva, G. L., Viscardy, S., Mège, D., Crismani, M. M. J., Aoki, S., et al. (2021). Probing the atmospheric Cl isotopic ratio on Mars: Implications for planetary evolution and atmospheric chemistry. *Geophysical Research Letters*, *48*(9), e2021GL092650. https://doi.org/10.1029/2021GL092650

Luginin, M., Trokhimovskiy, A., Taysum, B., Fedorova, A. A., Korablev, O., Olsen, K. S., et al. (2024). Evidence of rapid hydrogen chloride uptake on water ice in the atmosphere of Mars. *Icarus*, *411*, 115960. https://doi.org/10.1016/j.icarus.2024.115960

Madeleine, J.-B., Forget, F., Millour, E., Montabone, L., & Wolff, M. J. (2011). Revisiting the radiative impact of dust on Mars using the LMD global climate model. *Journal of Geophysical Research*, *116*(E11), E11010. https://doi.org/10.1029/2011JE003855

Mahaffy, P. R., Webster, C. R., Atreya, S. K., Franz, H., Wong, M., Conrad, P. G., et al. (2013). Abundance and isotopic composition of gases in the Martian atmosphere from the curiosity rover. *Science*, *341*(6143), 263–266. https://doi.org/10.1126/science.1237966

McAdam, A. C., Franz, H. B., Sutter, B., Archer, P. D., Jr., Freissinet, C., Eigenbrode, J. L., et al. (2014). Sulfur-bearing phases detected by evolved gas analysis of the Rocknest aeolian deposit, gale crater, Mars. *Journal of Geophysical Research: Planets*, *119*(2), 373–393. https://doi.org/10.1002/2013JE004518

McKeachie, J. R., Appel, M. F., Kirchner, U., Schindler, R. N., & Benter, T. (2004). Observation of a heterogeneous source of OClO from the reaction of ClO radicals on ice. *The Journal of Physical Chemistry B*, *108*(43), 16786–16797. https://doi.org/10.1021/jp049314p

21699100, 2025, 11, Downloaded from https://agupubs.onlinelibrary.wiley.com/doi/10.1029/2025JE009105 by Sara Faggi - Nasa Goddard , Wiley Online Library on [14/11/2025]. See the Terms and Conditions (https://onlinelibrary.wiley.com/terms-and-conditions) on Wiley Online Library for rules of use; OA articles are governed by the applicable Creative Commons License

Michelsen, H. A., Salawitch, R. J., Gunson, M. R., Aellig, C., Kämpfer, N., Abbas, M. M., et al. (1996). Stratospheric chlorine partitioning: Constraints from shuttle-borne measurements of [HCl], [ClNO3], and [ClO]. *Geophysical Research Letters*, *23*(17), 2361–2364. https://doi.org/10.1029/96GL00787

Millour, E., Forget, F., Spiga, A., Pierron, T., Bierjon, A., Montabone, L., et al. (2015). The Mars climate database. https://doi.org/10.5194/epsc2024-516

Montabone, L., Edwards, C. S., Forget, F., Kass, D., Kleinboehl, A., Guha, B. K., et al. (2024). Monitoring Martian atmospheric dust using multi-annual, multi-instrument orbital observations. *LPI Contributions*, *3007*, 3513.

Montabone, L., Forget, F., Millour, E., Wilson, R. J., Lewis, S. R., Cantor, B., et al. (2015). Eight-year climatology of dust optical depth on Mars. *Icarus*, *251*, 65–95. https://doi.org/10.1016/j.icarus.2014.12.034

Montabone, L., Spiga, A., Kass, D. M., Kleinböhl, A., Forget, F., & Millour, E. (2020). Martian year 34 column dust climatology from Mars climate sounder observations: Reconstructed maps and model simulations. *Journal of Geophysical Research: Planets*, *125*(8), e2019JE006111. https://doi.org/10.1029/2019JE006111

Montmessin, F., Belyaev, D. A., Lefèvre, F., Alday, J., Vals, M., Fedorova, A. A., et al. (2022). Reappraising the production and transfer of hydrogen atoms from the middle to the upper atmosphere of Mars at times of elevated water vapor. *Journal of Geophysical Research: Planets*, *127*(5), e2022JE007217. https://doi.org/10.1029/2022JE007217

Montmessin, F., Fedorova, A., Alday, J., Aoki, S., Chaffin, M., Chaufray, J.-Y., et al. (2024). Mars' water cycle and escape: A view from Mars express and beyond. *Space Science Reviews*, *220*(7), 77. https://doi.org/10.1007/s11214-024-01099-6

Montmessin, F., Forget, F., Rannou, P., Cabane, M., & Haberle, R. M. (2004). Origin and role of water ice clouds in the Martian water cycle as inferred from a general circulation model. *Journal of Geophysical Research*, *109*(E10). https://doi.org/10.1029/2004JE002284

Montmessin, F., Smith, M. D., Langevin, Y., Mellon, M. T., & Fedorova, A. (2017). The water cycle. In F. Forget, M. D. Smith, R. T. Clancy, R. W. Zurek, & R. M. Haberle (Eds.), *The atmosphere and climate of Mars* (pp. 338–373). Cambridge University Press. https://doi.org/10.1017/9781139060172.011

Olsen, K. S., Fedorova, A. A., Kass, D. M., Kleinböhl, A., Trokhimovskiy, A., Korablev, O. I., et al. (2024a). Relationships between HCl, H2O, aerosols, and temperature in the martian atmosphere: 1. Climatological outlook. *Journal of Geophysical Research: Planets*, *129*(8), e2024JE008350. https://doi.org/10.1029/2024JE008350

Olsen, K. S., Fedorova, A. A., Kass, D. M., Kleinböhl, A., Trokhimovskiy, A., Korablev, O. I., et al. (2024b). Relationships between HCl, H2O, aerosols, and temperature in the martian atmosphere: 2. Quantitative correlations. *Journal of Geophysical Research: Planets*, *129*(8), e2024JE008351. https://doi.org/10.1029/2024JE008351

Olsen, K. S., Trokhimovskiy, A., Montabone, L., Fedorova, A. A., Luginin, M., Lefèvre, F., et al. (2021). Seasonal reappearance of HCl in the atmosphere of Mars during the Mars year 35 dusty season. *Astronomy and Astrophysics*, *647*, A161. https://doi.org/10.1051/0004-6361/202140329

Osterloo, M. M., Hamilton, V. E., Bandfield, J. L., Glotch, T. D., Baldridge, A. M., Christensen, P. R., et al. (2008). Chloride-bearing materials in the Southern highlands of Mars. *Science*, *319*(5870), 1651–1654. https://doi.org/10.1126/science.1150690

Pollack, J. B., Colburn, D. S., Flasar, F. M., Kahn, R., Carlston, C. E., & Pidek, D. (1979). Properties and effects of dust particles suspended in the Martian atmosphere. *Journal of Geophysical Research*, *84*(B6), 2929–2945. https://doi.org/10.1029/JB084iB06p02929

Rajendran, K., Streeter, P. M., Lewis, S. R., Duffy, M. K. D., Holmes, J. A., Olsen, K. S., et al. (2025). Global transport of chlorine species in the martian atmosphere and the resulting surface distribution of perchlorates. *Journal of Geophysical Research: Planets*, *130*(3), e2024JE008537. https://doi.org/10.1029/2024JE008537

Rayner, J., Bond, T., Bonnet, M., Jaffe, D., Muller, G., & Tokunaga, A. (2012). iSHELL: A 1-5 micron cross-dispersed R=70,000 immersion grating spectrograph for IRTF. *Ground-Based and Airborne Instrumentation for Astronomy*, *IV*(8446), 832–843. https://doi.org/10.1117/12.925511

Rayner, J., Tokunaga, A., Jaffe, D., Bond, T., Bonnet, M., Ching, G., et al. (2022). iSHELL: A 1–5 micron R = 80,000 immersion grating spectrograph for the NASA infrared telescope facility. *Publications of the Astronomical Society of the Pacific*, *134*(1031), 015002. https://doi.org/10.1088/1538-3873/ac3cb4

Savijärvi, H., Harri, A.-M., & Kemppinen, O. (2016). The diurnal water cycle at curiosity: Role of exchange with the regolith. *Icarus*, *265*, 63–69. https://doi.org/10.1016/j.icarus.2015.10.008

Sholes, S. F., Smith, M. L., Claire, M. W., Zahnle, K. J., & Catling, D. C. (2017). Anoxic atmospheres on Mars driven by volcanism: Implications for past environments and life. *Icarus*, *290*, 46–62. https://doi.org/10.1016/j.icarus.2017.02.022

Smith, M. D. (2002). The annual cycle of water vapor on Mars as observed by the thermal emission spectrometer. *Journal of Geophysical Research*, *107*(E11), 25-1–25-19. https://doi.org/10.1029/2001JE001522

Smith, M. D. (2008). Spacecraft observations of the martian atmosphere. *Annual Review of Earth and Planetary Sciences*, *36*(1), 191–219. https://doi.org/10.1146/annurev.earth.36.031207.124334

Smith, M. D., Badri, K., Atwood, S. A., Edwards, C. S., Christensen, P. R., Wolff, M. J., et al. (2022). EMIRS observations of the aphelion-season Mars atmosphere. *Geophysical Research Letters*, *49*(15), e2022GL099636. https://doi.org/10.1029/2022GL099636

Smith, M. D., Daerden, F., Neary, L., & Khayat, A. (2018). The climatology of carbon monoxide and water vapor on Mars as observed by CRISM and modeled by the GEM-Mars general circulation model. *Icarus*, *301*, 117–131. https://doi.org/10.1016/j.icarus.2017.09.027

Smith, M. D., Pearl, J. C., Conrath, B. J., & Christensen, P. R. (2001). One martian year of atmospheric observations by the thermal emission spectrometer. *Geophysical Research Letters*, *28*(22), 4263–4266. https://doi.org/10.1029/2001GL013608

Smith, M. D., Wolff, M. J., Spanovich, N., Ghosh, A., Banfield, D., Christensen, P. R., et al. (2006). One martian year of atmospheric observations using MER Mini-TES. *Journal of Geophysical Research*, *111*(E12). https://doi.org/10.1029/2006JE002770

Smith, M. L., Claire, M. W., Catling, D. C., & Zahnle, K. J. (2014). The formation of sulfate, nitrate and perchlorate salts in the martian atmosphere. *Icarus*, *231*, 51–64. https://doi.org/10.1016/j.icarus.2013.11.031

Solomon, S. (1999). Stratospheric ozone depletion: A review of concepts and history. *Reviews of Geophysics*, *37*(3), 275–316. https://doi.org/10.1029/1999RG900008

Solomon, S. C., Aharonson, O., Aurnou, J. M., Banerdt, W. B., Carr, M. H., Dombard, A. J., et al. (2005). New perspectives on ancient Mars. *Science*, *307*(5713), 1214–1220. https://doi.org/10.1126/science.1101812

Squyres, S. W., Arvidson, R. E., Bollen, D., Bell III, J. F., Brückner, J., Cabrol, N. A., et al. (2006). Overview of the opportunity Mars exploration Rover mission to meridiani planum: Eagle crater to purgatory ripple. *Journal of Geophysical Research*, *111*(E12). https://doi.org/10.1029/2006JE002771

Steele, L. J., Balme, M. R., Lewis, S. R., & Spiga, A. (2017). The water cycle and regolith–atmosphere interaction at gale crater, Mars. *Icarus*, *289*, 56–79. https://doi.org/10.1016/j.icarus.2017.02.010

21699100, 2025, 11, Downloaded from https://agupubs.onlinelibrary.wiley.com/doi/10.1029/2025JE009105 by Sara Faggi - Nasa Goddard , Wiley Online Library on [14/11/2025]. See the Terms and Conditions (https://onlinelibrary.wiley.com/terms-and-conditions) on Wiley Online Library for rules of use; OA articles are governed by the applicable Creative Commons License

Streeter, P. M., Rajendran, K., Lewis, S. R., Olsen, K. S., Trokhimovskiy, A., Korablev, O., & Patel, M. R. (2025). Global distribution and seasonality of Martian atmospheric HCl explained through heterogeneous chemistry. *Geophysical Research Letters*, *52*(6), e2024GL111059. https://doi.org/10.1029/2024GL111059

Taysum, B. M., Palmer, P. I., Olsen, K., Luginin, M., Ignatiev, N., Trokhimovskiy, A., et al. (2024a). Observed seasonal changes in Martian hydrogen chloride explained by heterogeneous chemistry. *Astronomy and Astrophysics*, *687*, A191. https://doi.org/10.1051/0004-6361/202449546

Taysum, B. M., Palmer, P. I., Olsen, K., Luginin, M., Ignatiev, N., Trokhimovskiy, A., et al. (2024b). Observed seasonal changes in Martian hydrogen chloride explained by heterogeneous chemistry. *Astronomy and Astrophysics*, *687*, A191. https://doi.org/10.1051/0004-6361/202449546

Toulmin III, P., Baird, A. K., Clark, B. C., Keil, K., Rose, H. J., Jr., Christian, R. P., et al. (1977). Geochemical and mineralogical interpretation of the viking inorganic chemical results. *Journal of Geophysical Research (1896-1977)*, *82*(28), 4625–4634. https://doi.org/10.1029/JS082i028p04625

Trokhimovskiy, A., Fedorova, A. A., Olsen, K. S., Alday, J., Korablev, O., Montmessin, F., et al. (2021). Isotopes of chlorine from HCl in the Martian atmosphere. *Astronomy and Astrophysics*, *651*, A32. https://doi.org/10.1051/0004-6361/202140916

Trokhimovskiy, A., Fedorova, A., Korablev, O., Montmessin, F., Bertaux, J.-L., Rodin, A., & Smith, M. D. (2015). Mars' water vapor mapping by the SPICAM IR spectrometer: Five martian years of observations. *Icarus*, *251*, 50–64. https://doi.org/10.1016/j.icarus.2014.10.007

Vandaele, A. C., Aoki, S., Bauduin, S., Daerden, F., Fedorova, A., Giuranna, M., et al. (2024). Composition and chemistry of the martian atmosphere as observed by Mars express and ExoMars trace gas orbiter. *Space Science Reviews*, *220*(7), 75. https://doi.org/10.1007/s11214-024-01109-7

Villanueva, G. L., DiSanti, M. A., Mumma, M. J., & Xu, L.-H. (2012a). A quantum band model of the ν3 fundamental of methanol (ch3oh) and its application to fluorescence spectra of comets. *The Astrophysical Journal*, *747*(1), 37. https://doi.org/10.1088/0004-637X/747/1/37

Villanueva, G. L., Faggi, S., & Liuzzi, G. (2023). astroPSG: Advanced python package for processing and analyzing spectroscopic data (version v1.0) [Computer software]. *Zenodo*. https://doi.org/10.5281/zenodo.10059232

Villanueva, G. L., Liuzzi, G., Aoki, S., Stone, S. W., Brines, A., Thomas, I. R., et al. (2022a). The deuterium isotopic ratio of water released from the Martian caps as measured with TGO/NOMAD. *Geophysical Research Letters*, *49*(12), e2022GL098161. https://doi.org/10.1029/2022GL098161

Villanueva, G. L., Liuzzi, G., Faggi, S., Protopapa, S., Kofman, V., Fauchez, T., et al. (2022b). Fundamentals of the planetary spectrum generator. Retrieved from https://psg.gsfc.nasa.gov/help.php#handbook

Villanueva, G. L., Mumma, M. J., Bonev, B. P., Novak, R. E., Barber, R. J., & DiSanti, M. A. (2012b). Water in planetary and cometary atmospheres: H2O/HDO transmittance and fluorescence models. *Journal of Quantitative Spectroscopy and Radiative Transfer*, *113*(3), 202–220. https://doi.org/10.1016/j.jqsrt.2011.11.001

Villanueva, G. L., Mumma, M. J., DiSanti, M. A., Bonev, B. P., Gibb, E. L., Magee-Sauer, K., et al. (2011). The molecular composition of comet C/2007 W1 (Boattini): Evidence of a peculiar outgassing and a rich chemistry. *Icarus*, *216*(1), 227–240. https://doi.org/10.1016/j.icarus.2011.08.024

Villanueva, G. L., Mumma, M. J., Novak, R. E., Käufl, H. U., Hartogh, P., Encrenaz, T., et al. (2015). Strong water isotopic anomalies in the martian atmosphere: Probing current and ancient reservoirs. *Science*, *348*(6231), 218–221. https://doi.org/10.1126/science.aaa3630

Villanueva, G. L., Mumma, M. J., Novak, R. E., Radeva, Y. L., Käufl, H. U., Smette, A., et al. (2013). A sensitive search for organics (CH4, CH3OH, H2CO, C2H6, C2H2, C2H4), hydroperoxyl (HO2), nitrogen compounds (N2O, NH3, HCN) and chlorine species (HCl, CH3Cl) on Mars using ground-based high-resolution infrared spectroscopy. *Icarus*, *223*(1), 11–27. https://doi.org/10.1016/j.icarus.2012.11.013

Villanueva, G. L., Smith, M. D., Protopapa, S., Faggi, S., & Mandell, A. M. (2018). Planetary Spectrum Generator: An accurate online radiative transfer suite for atmospheres, comets, small bodies and exoplanets. *Journal of Quantitative Spectroscopy and Radiative Transfer*, *217*, 86–104. https://doi.org/10.1016/j.jqsrt.2018.05.023

Wang, A., Yan, Y., Jolliff, B. L., McLennan, S. M., Wang, K., Shi, E., & Farrell, W. M. (2020). Chlorine release from common chlorides by Martian dust activity. *Journal of Geophysical Research: Planets*, *125*(6), e2019JE006283. https://doi.org/10.1029/2019JE006283

Wilson, E. H., Atreya, S. K., Kaiser, R. I., & Mahaffy, P. R. (2016). Perchlorate formation on Mars through surface radiolysis-initiated atmospheric chemistry: A potential mechanism. *Journal of Geophysical Research: Planets*, *121*(8), 1472–1487. https://doi.org/10.1002/2016JE005078

Zahnle, K., Haberle, R. M., Catling, D. C., & Kasting, J. F. (2008). Photochemical instability of the ancient Martian atmosphere. *Journal of Geophysical Research*, *113*(E11). https://doi.org/10.1029/2008JE003160

21699100, 2025, 11, Downloaded from https://agupubs.onlinelibrary.wiley.com/doi/10.1029/2025JE009105 by Sara Faggi - Nasa Goddard , Wiley Online Library on [14/11/2025]. See the Terms and Conditions (https://onlinelibrary.wiley.com/terms-and-conditions) on Wiley Online Library for rules of use; OA articles are governed by the applicable Creative Commons License